RESEARCH ARTICLE

Facile synthesis of cadmium-doped graphite carbon nitride for photocatalytic degradation of tetracycline under visible light irradiation

Yin Zhao[1,2] · Hong Qin[1,2] · Ziwei Wang[1,2] · Han Wang[1,2] · Yangzhuo He[1,2] · Quyang Tian[1,2] · Qianlan Luo[3] · Piao Xu[1,2]

Abstract

In recent years, using semiconductor photocatalysts for antibiotic contaminant degradation under visible light has become a hot topic. Herein, a novel and ingenious cadmium-doped graphite phase carbon nitride (Cd-g-C_3N_4) photocatalyst was successfully constructed via the thermal polymerization method. Experimental and characterization results revealed that cadmium (Cd) was well doped at the g-C_3N_4 surface and exhibited high intercontact with g-C_3N_4. Additionally, the introduction of cadmium significantly improved the photocatalytic activity, and the optimum degradation efficiency of tetracycline (TC) reached 98.1%, which was exceeded 2.0 times that of g-C_3N_4 (43.9%). Meanwhile, the Cd-doped sample presented a higher efficiency of electrical conductivity, light absorption property, and photogenerated electron-hole pair migration compared with g-C_3N_4. Additionally, the quenching experiments and electron spin-resonance tests exhibited that holes (h^+), hydroxyl radicals ($\bullet OH$), superoxide radicals ($\bullet O_2^-$) were the main active species involved in TC degradation. The effects of various conditions on photocatalytic degradation, such as pH, initial TC concentrations, and catalyst dosage, were also researched. Finally, the degradation mechanism was elaborated in detail. This work gives a reasonable point to synthesizing high-efficiency and economic metal-doped photocatalysts.

Introduction

For the past few years, the environmental problems were overwhelming with the continuous increase in population and medical industry (Abbott 2010; McCauley and Stephens 2012; Wang and Yang 2016). Especially, the reckless discharge of untreated wastewater and sewage makes antibiotic pollutants accumulate in water. Tetracycline (TC), the most common antibiotic contaminant with a huge threat to the water environment and human health, was frequently detected in the water environment. Thus, it is necessary to seek a green and efficient technology to degrade antibiotic TC pollution in water.

Photocatalysis technology, as an environmental-friendly process, has become a promising method applied in the energy and environmental remediation field (Ge et al. 2011; Liu et al. 2016; Wang et al. 2008; Zhu et al. 2017). The most important tasks in photocatalysis technology are designing high-efficient, non-toxic, and low-cost photocatalysts (Xiang et al. 2012). Recently, metallic oxides, metallic nitrides, and metallic sulfides have been developed as excellent photocatalytic materials to remove antibiotic pollutants (Chan et al. 2017; Shi et al. 2018; Song et al. 2019; Wang et al. 2018b; Xu et al. 2019). However, some obvious defects, such as high cost, low light absorption efficiency, and photo-corrosion, have hindered their further application (Yan et al. 2010; Yu and Wang 2015; Yuan et al. 2014; Zhao et al. 2014).

✉ Piao Xu
piaoxu@hnu.edu.cn

1 College of Environmental Science and Engineering, Hunan University, Lushan South Road, Yuelu District, Changsha 410082, People's Republic of China

2 Key Laboratory of Environmental Biology and Pollution Control (Hunan University), Ministry of Education, Lushan South Road, Yuelu District, Changsha 410082, People's Republic of China

3 Changsha Liuyang Eco-environmental Monitoring Station, No. 1 Fuxing Middle Road in Liuyang, Changsha, People's Republic of China

In comparison, graphite phase carbon nitride (g-C$_3$N$_4$), as a metal-free conjugate semiconductor, is considered one of the most promising photocatalysts than metallic photocatalysts (Wang et al. 2008; Lu et al. 2015; Zhou et al. 2013). The high physicochemical stability, tunable electronic structure, and appropriate bandgap for absorbing blue light of g-C$_3$N$_4$ make g-C$_3$N$_4$ receive much attention and are widely used in antibiotic pollutant degradation (Butchosa et al. 2014; Chen et al. 2020; Liu et al. 2015; Wang et al. 2020a; Wang et al. 2019; Wang et al. 2020b; Yan et al. 2009a). Nevertheless, the photodegradation properties have been limited by several disadvantages of g-C$_3$N$_4$, such as insufficient light absorption, low surface area, and rapid recombination rate of photogenerated carriers (Li et al. 2009a; Chang et al. 2018; Zhang and Xia 2011).

Several strategies, including chemical doping, morphological control, electronic structural design, and defects engineering, have been explored to overcome the shortcomings of g-C$_3$N$_4$ (Gao et al. 2012; Katsumata et al. 2014; Ou et al. 2015; Qi et al. 2018). Among these strategies, metal element doping of g-C$_3$N$_4$ has been commonly regarded as a feasible method to improve photodegradation properties (Schwinghammer et al. 2014; Tahir et al. 2013; Thaweesak et al. 2017; Wang et al. 2018b). Metal element doping influenced the redox capacity, morphology, and crystal phase structure of semiconductors (Xiong et al. 2016; Gao et al. 2013; Ong et al. 2016; Wang et al. 2009a). Moreover, the light absorption ability and charge transfer efficiency of catalysts could be effectively improved via the metal doping method (Jun et al. 2013; Liu et al. 2012; Fan et al. 2019; Gao et al. 2012; Huang et al. 2019; Zhu et al. 2017).

To the best of our knowledge, there is rarely reported Cd-g-C$_3$N$_4$ for photocatalytic degradation. Herein, the soluble cadmium ion and g-C$_3$N$_4$ precursor were fully mixed by an ingenious pretreated oil bath, and the cadmium-doped graphite phase carbon nitride (Cd-g-C$_3$N$_4$) photocatalyst was successfully constructed via further calcining. Different proportions of cadmium were introduced into g-C$_3$N$_4$ by changing the Cd content. The experimental and characterization results demonstrated that the photocatalytic performance, light absorption ability, and specific surface area of g-C$_3$N$_4$ were improved after cadmium doping. This study elaborated an innovative viewpoint for further chemistry-doped photocatalysts designed.

Experimental section

Chemicals

All the chemicals were of analytical grade. Cadmium chloride (CdCl$_2$), polyvinyl alcohol (PVA), melamine, tetracycline (TC), ethylenediaminetetraacetic acid disodium salt (EDTA-2Na), anhydrous ethanol, isopropanol (IPA), 4-hydroxy-2,2,6,6-tetramethyl piperidinyloxy (TEMPO), and deionized water (H$_2$O) were employed without further purification.

Synthesis of g-C$_3$N$_4$

The g-C$_3$N$_4$ powder was prepared via the traditional calcination method with little revision; the specific steps were as follows (Wang et al. 2021): weigh 10 g melamine and put into a porcelain alumina crucible covered with tin foil (50 mL). Then, the crucible was placed into a muff furnace with a heating rate of 10 °C/min and kept at 550 °C for 3 h. After the porcelain alumina crucible was cooled down to room temperature, the obtained g-C$_3$N$_4$ powder was grounded and collected for further use.

Synthesis of Cd-g-C$_3$N$_4$

All Cd-doped g-C$_3$N$_4$ samples were prepared through the thermal polymerization of melamine in the presence of CdCl$_2$. g-C$_3$N$_4$ sample of 1.0 g was taken and dissolved in 20 mL of ethanol/H$_2$O solution (15/5, vol/vol), and then different amounts of CdCl$_2$ was put into the solution. After ultrasound for half an hour, the solvent evaporated in an oil bath under magnetic agitation at 60 °C. Whereafter, the remaining solids were placed in a petri dish, covered with a plastic wrap, and desiccated in a vacuum-drying oven at 60 °C for 24 h. When cooled to room temperature, the obtained samples were poured into a mortar to thoroughly ground. Then, the samples were placed into a muff furnace with a heating rate of 10 °C/min, kept at 550 °C for 3 h. When the product was static cooled, the product was marked as X-Cd-g-C$_3$N$_4$ photocatalysts (X = 5, 10, 15) with different cadmium chloride contents. The cadmium chloride contents and exact cadmium contents in carbon nitride material samples are listed in Table S1, and the brief diagram of the 10-Cd-g-C$_3$N$_4$ prepared process is illustrated in Scheme S1.

Characterization

X-ray diffraction (XRD) was recorded by D8 advance via Cu-Kα radiation, the scan ranges of 2θ extended from 10 to 80° with a scan speed of 8°/min. The morphological structure was obtained on JSM-7800F scanning electron microscopy (SEM). Escalab 250Xi spectrometer via Al Kα X-ray source was employed to measure X-ray photoelectron spectroscopy (XPS). The morphologies of the catalyst were observed through Jeol 2100F transmission electron microscopy (TEM). The photoluminescence spectra (PL) were investigated by Fluoromax-4 spectrofluorometer at 380-nm excitation wavelength. Fourier transform infrared spectroscopy (FT-IR) was measured by Bruker spectrometer,

with the wavenumber ranging from 500 to 4000 cm^{-1}. Ultraviolet-visible diffuse reflectance absorption spectroscopy (UV-Vis DRS) was performed on Cary 300 UV-Vis spectrophotometer, scanning from 200 to 800 nm. The Brunauer–Emmett–Teller (BET) surface area was carried out by Micromeritics ASAP2460. Electrochemical impedance spectroscopy (ESR) was analyzed by Bruker a300. The total organic carbon (TOC) was tested via Analytikjena multi N/C 2100. The chemical element compositions were analyzed by the energy-dispersive spectroscopy (EDS) mapping images, captured on a Zeiss Sigma 300 atomic resolution analytical microscope.

Photocatalytic process

A 300 W Xenon lamp with a 420-nm pass filter was employed to simulate sunlight for the catalytic process. Typically, 0.04 g catalyst was weighed in a 100-mL beaker, and 50 mL TC solution at 10 mg/L was poured into the beaker and stirred at 450 rpm for photocatalysis studies. To eliminate the effect of adsorption, we placed the mixture solutions in the dark and stirred for 0.5 h until the adsorption-desorption equilibrium. After the light source was added, TC suspension was collected every 10 min with a 0.22-μm filter membrane. Then, the concentration of suspension was tested by UV-Vis spectrophotometer with a wavelength of 357 nm.

Photoelectrochemical process

The photoelectrochemical (PEC) test was conducted on the CHI0-660D workstation. A 300-W Xenon lamp with a 420-nm pass filter was used as the light source. The PEC performance of g-C$_3$N$_4$ and 10-Cd-g-C$_3$N$_4$ was evaluated

using a normal three-electrode system with a 0.2 M Na$_2$SO$_4$ solution. In the three-electrode system, Ag/AgCl electrode was the reference electrode, the Pt electrode was the counter electrode and the working electrode was fluorine-doped tin oxide (FTO) with diluted catalyst. The adhered process was depicted as follows: FTO was firstly ultrasonic cleaned in ethanol, acetone, and deionized water three times, respectively. Secondly, 10 mg catalyst was uniformly immersed into 150 uL naphthol for ultrasonic oscillation. Finally, 100 μL suspension was evenly dropped onto FTO and dried at 120 °C.

Results and discussion

Structure and morphology

The structure and crystalline phase were analyzed by XRD. Figure 1a illustrates the XRD spectra of g-C$_3$N$_4$ and 10-Cd-g-C$_3$N$_4$. For g-C$_3$N$_4$, two diffraction peaks were observed in the vicinity of 12.9° and 27.5°, which were in good agreement with the standard XRD pattern of graphitic carbon nitride (JCPDS 87-1526). The peak at 12.9° was confirmed by the in-planar tri-s-triazine structural ordering of the conjugated aromatic system, and the peak at 27.5° represented the inter-planar periodic lamellar ordering of typical graphite-like carbon nitride (Li et al. 2016). According to Bragg's Law, the distance between the in-plane layers was about 0.69 nm, and the distance between the inter-planar layers was about 0.33 nm (Lu et al. 2015; Zou et al. 2019). For the 10-Cd-g-C$_3$N$_4$ sample, the intensities of both two peaks were significantly abated, indicating that the reduced hydrogen bond effect and the strong electrostatic interactions between
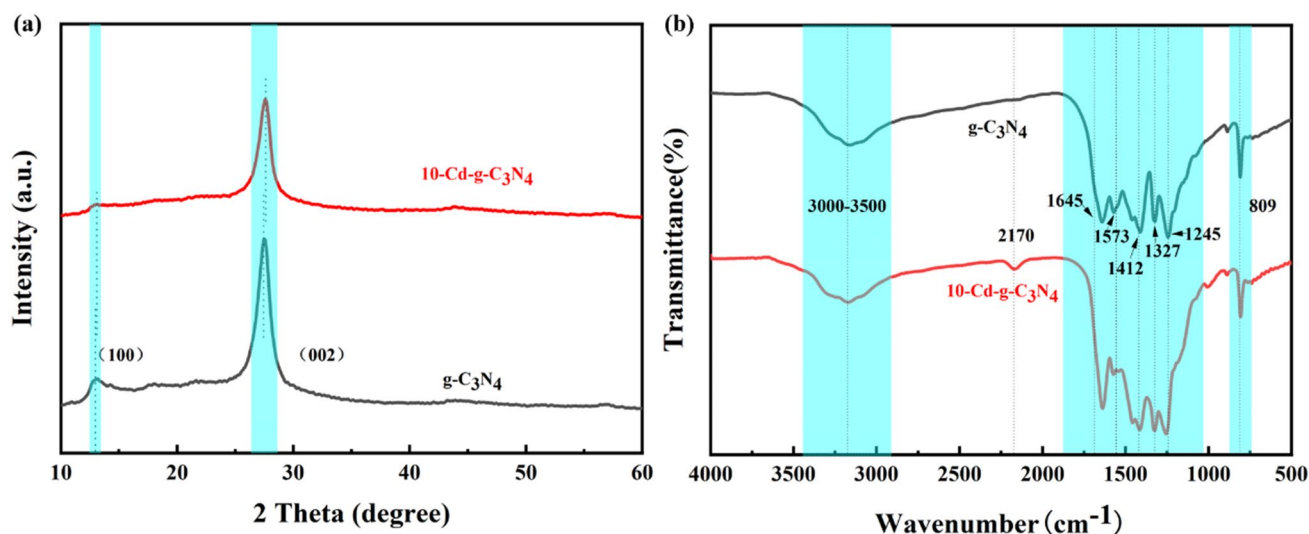

Fig. 1 **a** XRD patterns of g-C$_3$N$_4$ and 10-Cd-g-C$_3$N$_4$ photocatalyst; **b** FT-IR spectra of g-C$_3$N$_4$ and 10-Cd-g-C$_3$N$_4$ photocatalyst

Cd^{2+} and N for Cd^{2+} incorporated into the $g-C_3N_4$ lattice (Sher et al. 2021), as a consequence, the distance between the inter-planar layers of $g-C_3N_4$ was decreased (Thaweesak et al. 2017; Yu et al. 2016; Abu Hanif et al. 2021). Apparently, there was no peak of cadmium in the $10-Cd-g-C_3N_4$ sample, which was due to the small content and high dispersion of cadmium (Jia et al. 2019; Wang et al. 2020b).

The functional groups in the $g-C_3N_4$ and $10-Cd-g-C_3N_4$ determined by FT-IR are illustrated in Fig. 1b. As for $g-C_3N_4$, the wide region from 3000 to 3500 cm^{-1} was ascribed to the stretching mode of the partial hydrogenation of exposed nitrogen (N-H) and the adsorbed water molecules (O-H) (Tonda et al. 2014; Wang et al. 2018a; Yan et al. 2016). In the region of 1200–1700 cm^{-1}, five characteristic peaks (1245, 1327, 1412, 1573, and 1645 cm^{-1}, respectively) were found, indicating the distinctive stretching mode of aromatic C–N heterocycle (C_6N_7) (Park et al. 2011; Sobhana et al. 2011). The peak at 809 cm^{-1} was assigned to the typical out-of-plane bending vibration of the tri-s-triazine-based structure (Liu et al. 2020), which verified the presence of triazine units (Wang et al. 2018a; Yan et al. 2009b). Obviously, the $10-Cd-g-C_3N_4$ sample exhibited almost similar FT-IR features to $g-C_3N_4$, indicating the primary framework of $g-C_3N_4$ was well preserved after cadmium doping. Specifically, a weak peak was found in the region of 2170 cm^{-1}, which may assign to the additional stretching mode caused by the interaction of cadmium and $g-C_3N_4$ (Sher et al. 2021). Additionally, the stretching mode of the partial hydrogenation of exposed nitrogen (N-H) was shifted and weakened, which corresponded to the Cd dopant being incorporated into $g-C_3N_4$ (Yang et al. 2013; Li et al. 2016).

The morphologies of as-prepared samples were examined by SEM. For $g-C_3N_4$, a thick layered and porous structure was presented (Fig. 2a−b), and the layers were piled up in an irregular manner (Narkbuakaew and Sujaridworakun 2020). Also, there was a large cross-sectional area between layers, which could function as excellent doping sites (Sher et al. 2021). Different from $g-C_3N_4$, the $10-Cd-g-C_3N_4$ sample exhibited a thinner nanosheets structure (Fig. 2c−d), revealing the aggregated nanosheets of $g-C_3N_4$ were exfoliated after Cd doping (Abu Hanif et al. 2021). Moreover, there were some crystal particles scattered on the nanosheets, which might correspond to Cd dopant.

The detailed morphologies of as-prepared samples were further surveyed by TEM. In Fig. 3a−b, it could be apparently seen that $g-C_3N_4$ was transparent or non-transparent, and the black shadow was owing to the overlap of multilayered nanosheets. Simultaneously, as for $10-Cd-g-C_3N_4$, an ultrathin nanosheet structure with partial shadow was exhibited (Fig. 3c−d), confirming that the layered structure of $g-C_3N_4$ was exfoliated after Cd doping, which was beneficial for increasing specific surface area. The elemental mapping (Fig. 3e−i and Fig. S1a−e) illustrated that the Cd element was homo-dispersed at the surface of $g-C_3N_4$, suggesting the successful doping of Cd. Due to the electrostatic attraction, the electron-rich Cd was firmly anchored on the electron-unsaturated $g-C_3N_4$ surface, which illustrated that the cadmium was exhibited high intercontact with $g-C_3N_4$ (Zhang et al. 2016). The elements' weight ratio of the $10-Cd-g-C_3N_4$ sample is illustrated in Table S2, where the elements C was 25.73%, N was 61.98%, and Cd was 12.28%. The low concentration of Cd compared with other elements confirms the

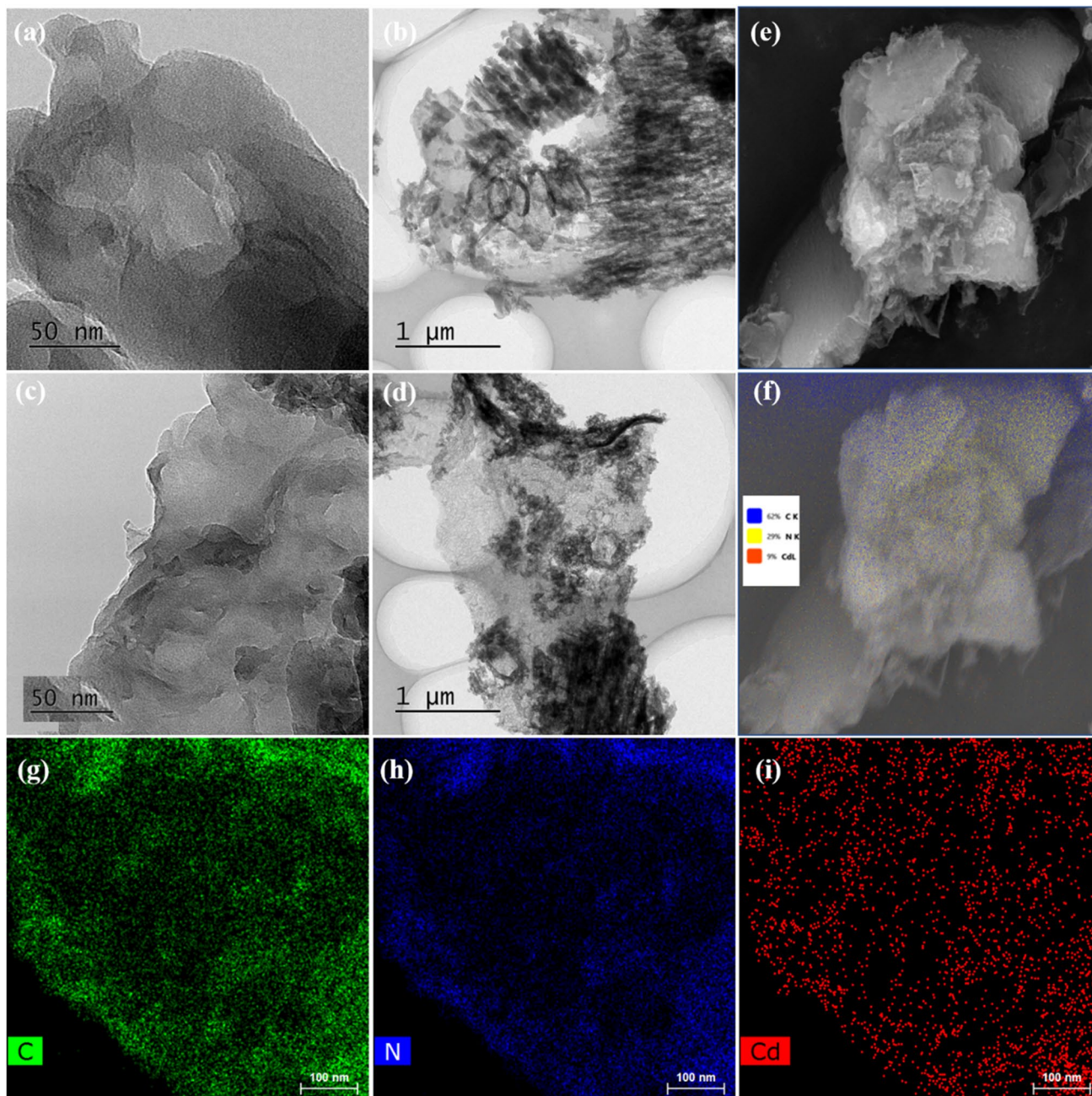**Fig. 2** SEM images of $g-C_3N_4$ (**a, b**) and $10-Cd-g-C_3N_4$ photocatalyst (**c, d**)
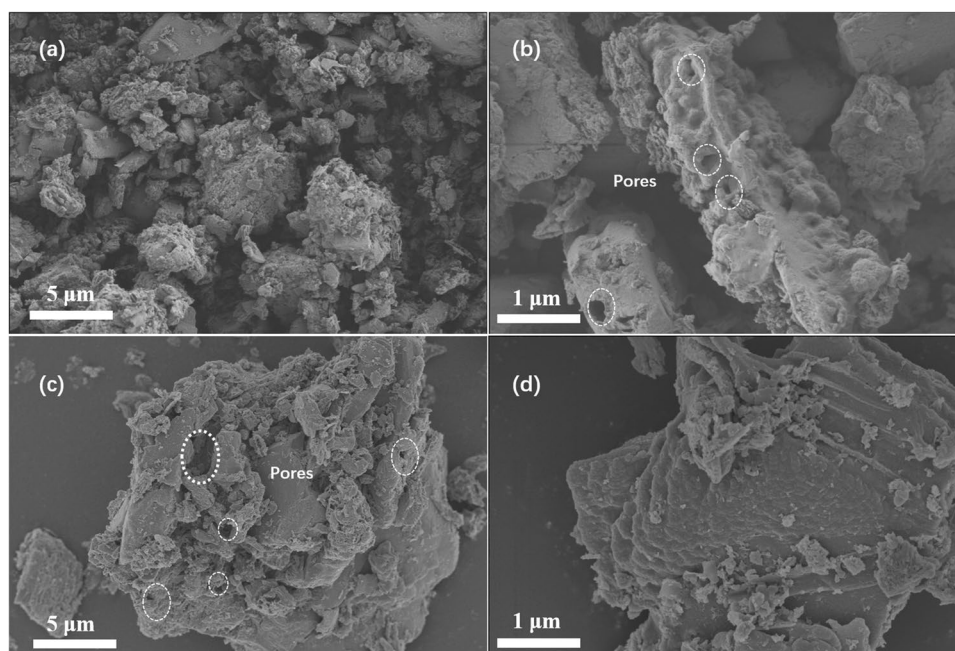
Fig. 3 TEM images of g-C_3N_4 (**a**, **b**) and 10-Cd-g-C_3N_4 photocatalyst (**c**, **d**). HAADF-STEM and element mapping (**e-i**) of 10-Cd-g-C_3N_4

cadmium doped on the g-C_3N_4 with a slight atomic ratio. The selected diffraction pattern (Fig. S1f) showed two distinct amorphous diffraction rings, which correspond to two peaks of carbon nitride in the XRD pattern. The energy-dispersive X-ray spectra (EDS) are illustrated in Fig. S1g, and only three peaks (C, N, Cd) were presented in the EDS mapping spectrum, confirming that the C, N, and Cd elements were homogeneous distribution and the prepared 10-Cd-g-C_3N_4 sample was highly pure. All these results clarified that 10-Cd-g-C_3N_4 samples were successfully constructed.

The specific surface area, pore volume, and pore size distribution were tested by BET, and the results are listed in Table S3. As exhibited in the N_2 adsorption-desorption isotherm (Fig. S2), the g-C_3N_4 and 10-Cd-g-C_3N_4 were type IV curves with H3 hysteresis hoop, which represented the presence of slit-shaped mesoporous structure (Iqbal et al. 2017). The specific surface area, pore volume, and pore size of g-C_3N_4 were 13.467 m^2/g, 0.077 cm^3/g, and 22.131 nm, respectively. After Cd doping, the specific surface area, pore volume, and pore size of 10-Cd-g-C_3N_4 were 16.46 m^2/g,

0.123 cm^3/g, and 25.917 nm, respectively. The 10-Cd-g-C$_3$N$_4$ sample obtained a larger surface area and pore volume than g-C$_3$N$_4$. Undoubtedly, a larger surface area and pore volume could provide more reaction active sites, increase light absorption area, and accelerate the transfer of photogenerated carriers, thus achieving a higher photocatalytic degradation rate (Chang et al. 2015).

The chemical element compositions and electronic structure details were investigated by XPS analysis. Figure 4a characterizes the full survey spectrum of g-C$_3$N$_4$ and 10-Cd-g-C$_3$N$_4$. Obviously, the g-C$_3$N$_4$ sample consisted of carbon (C), nitrogen (N), and oxygen (O) elements, while the 10-Cd-g-C$_3$N$_4$ sample consisted of C, N, O, and cadmium (Cd) elements. The presence of the O element in both g-C$_3$N$_4$ and 10-Cd-g-C$_3$N$_4$ samples was caused by the

surface absorption of water in the carbon nitride thermal polymerization process (Chou et al. 2016; Fang et al. 2016; Xue et al. 2019). No sign of chlorine (Cl) element (around 200 eV) could be observed in the 10-Cd-g-C$_3$N$_4$ sample since the Cl element was evaporated during the heating process (Amirthaganesan et al. 2010).

As exhibited in the high-resolution Cd 3d spectra of 10-Cd-g-C$_3$N$_4$ (Fig. 4b), two peaks situated at 412.4 eV and 405.6 eV were ascribed to the Cd 3d$_{5/2}$ and Cd 3d$_{3/2}$, respectively (Reddy et al. 2021), further confirming the presence of Cd^{2+} (Abu Hanif et al. 2021). Figure 4c elucidates the high-resolution C1s spectra of g-C$_3$N$_4$ and 10-Cd-g-C$_3$N$_4$. For g-C$_3$N$_4$, two sharp peaks were situated at 288.3 eV and 284.8 eV, respectively. The former peak at 288.4 eV resulted from sp^2 C atoms bonded with adjacent N atoms inside the
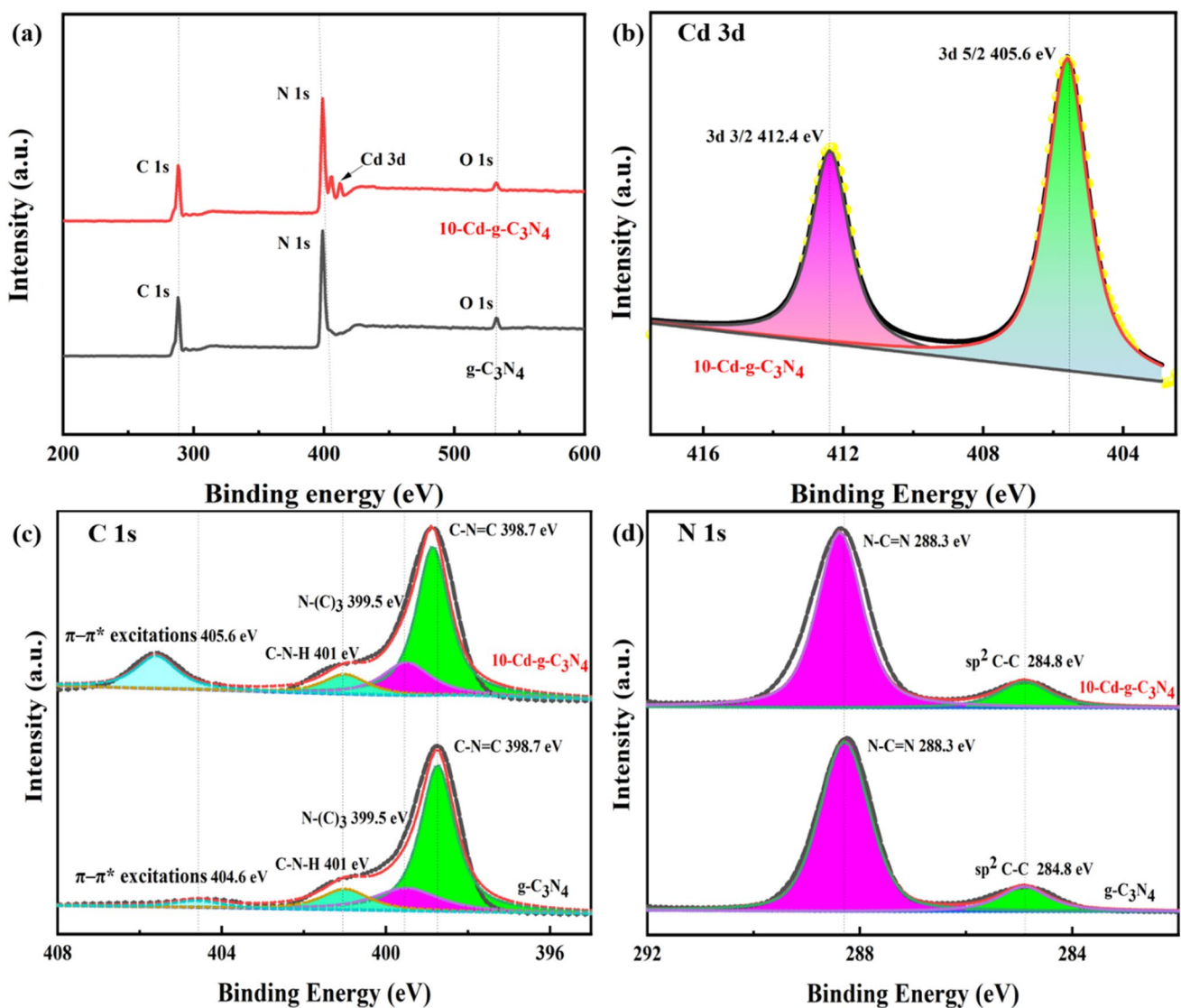

Fig. 4 XPS spectra of g-C$_3$N$_4$ and 10-Cd-g-C$_3$N$_4$ photocatalyst. **a** Full survey spectrum, **b** high-resolution Cd 3d, **c** high-resolution C 1s, **d** high-resolution N 1s

aromatic structure (N-C=N) (Thomas et al. 2008), and the latter peak at 284.8 eV was specifically on behalf of C-C bonds (Liu et al. 2010; Takanabe et al. 2010). Obviously, the 10-Cd-g-C_3N_4 sample indicated similar C1s spectra with g-C_3N_4. The high-resolution N 1s spectra of g-C_3N_4 and 10-Cd-g-C_3N_4 are shown in Fig. 4d. For g-C_3N_4, four peaks could be observed at 404.6 eV, 401 eV, 399.5 eV, and 398.7 eV. The peak at 404.6 eV was assigned to the effects of surface charge localization in the heterocycles or the π–π* excitations between the stacking interlayers (Kong et al. 2018; Li et al. 2018; Zhang et al. 2014; Zhang et al. 2012). The peak at 401 eV corresponded to amino groups (C-N-H) from the surface uncondensed bridging N atom (Liu et al. 2010; Thomas et al. 2008). The peak at 399.5 eV corresponded to N-$(C)_3$ groups, and the peak at 398.7 eV was originated from sp^2-bonded N atoms in triazine units (C=N-C) (Li et al. 2009b; Takanabe et al. 2010), which were similar to previously published literature (Chao et al. 2014; Matanović et al. 2015). Different from g-C_3N_4, the peak corresponding to the effects of surface charge localization in the heterocycles or the π–π* excitations between the stacking interlayers were shifted to 405.6 eV in the 10-Cd-g-C_3N_4 sample, which could explain by the interactions between Cd^{2+} and N of s-triazine-based unit (Soliman et al. 2019; Tarulli et al. 2006). Simultaneously, both C 1s and N 1s spectra of the 10-Cd-g-C_3N_4 sample exhibited an upwards

shifted compared with g-C_3N_4. All these positive shifts could be ascribed to the electrons transfer of the 10-Cd-g-C_3N_4 sample, further proving the strong electrostatic interaction between Cd elements and g-C_3N_4 (Ji et al. 2019; Yan et al. 2019).

Optical properties

The optical absorption ability was an evaluation criterion for optical properties, which could affect the electronic band structures of catalyst and further affect photocatalytic performance. The optical absorption ability of g-C_3N_4 and 10-Cd-g-C_3N_4 was revealed by the UV–vis diffuse adsorption spectrum (Fig. 5a). Obviously, an absorption threshold was found at 465 nm in g-C_3N_4, while the absorption threshold of 10-Cd-g-C_3N_4 had a significant redshift compared with g-C_3N_4, which illustrated that Cd doping may increase the light absorption ability and cause a narrower bandgap (Abu Hanif et al. 2021). Moreover, for the 10-Cd-g-C_3N_4 sample, the intensity of visible light adsorption was significantly enhanced than g-C_3N_4, which further confirmed the improvement of light absorption performance (Chen et al. 2021). The UV–vis diffuse adsorption spectrum of other samples with different cadmium contents is clarified in Fig. S3. Among these samples, the 10-Cd-g-C_3N_4 sample displayed the highest visible light absorption performance.
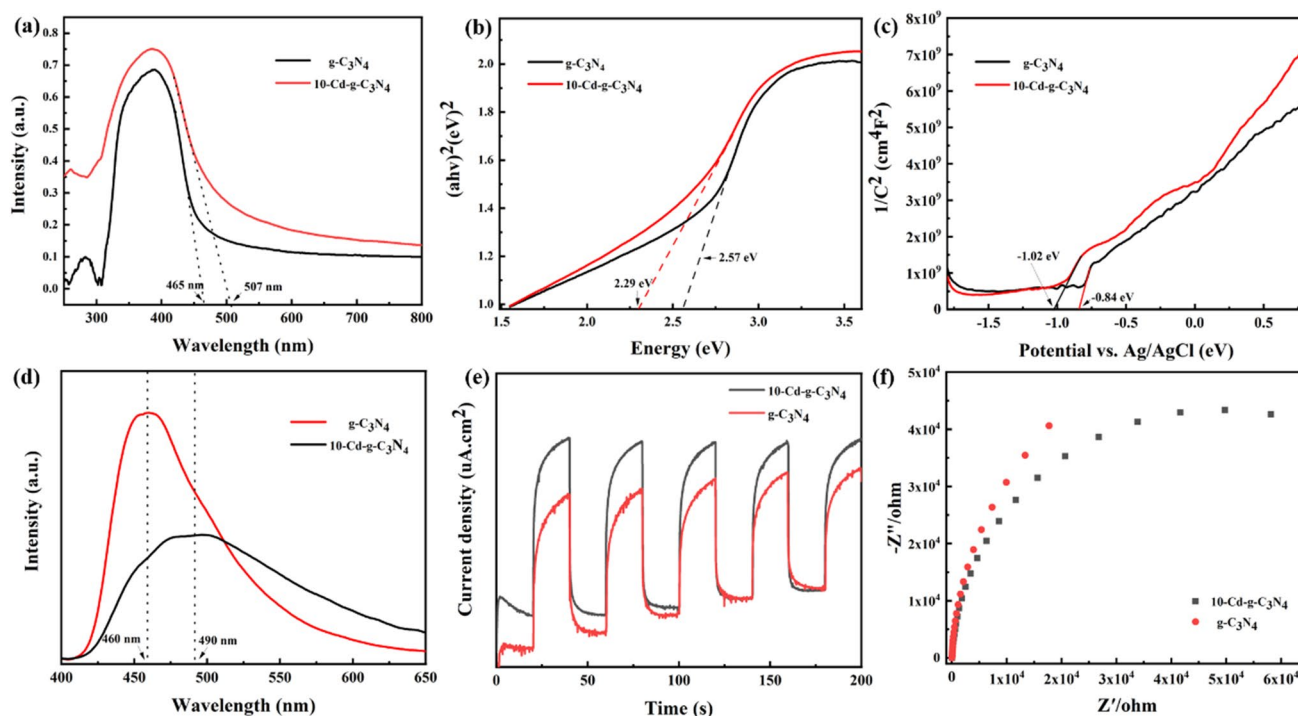

Fig. 5 **a** UV–vis diffuse reflectance spectra (DRS) and **b** band gap of g-C_3N_4 and 10-Cd-g-C_3N_4 photocatalyst. **c** Mott–Schottky plots and **d** the PL spectra of g-C_3N_4 and 10-Cd-g-C_3N_4 photocatalyst. **e** Photocurrent response spectra and **f** EIS Nyquist plots of g-C_3N_4 and 10-Cd-g-C_3N_4 photocatalyst

Both g-C$_3$N$_4$ and 10-Cd-g-C$_3$N$_4$ are direct-gaps semiconductors (Luo et al. 2017). The band gaps of g-C$_3$N$_4$ and 10-Cd-g-C$_3$N$_4$ were calculated based on the related Tauc plots. As shown in Fig. 5b, the band gaps (E$_g$) of g-C$_3$N$_4$ and 10-Cd-g-C$_3$N$_4$ were 2.57 eV and 2.29 eV. Notably, the Cd doping sample cause a narrower bandgap; undoubtedly, the narrower bandgap could reduce the excitation energy for photogenerated carriers, which was conducive to increasing the generation of electron-hole pairs, thus leading to a significant improvement in the visible light response (Kong et al. 2018; Wang et al. 2009b; Zhang et al. 2012; Ge et al. 2012).

The band potentials were ascertained by Mott-Schottky plots at 1000 Hz (Fig. 5c). Both g-C$_3$N$_4$ and 10-Cd-g-C$_3$N$_4$ displayed a positive Mott-Schottky slope, indicating g-C$_3$N$_4$ and 10-Cd-g-C$_3$N$_4$ were both n-type semiconductors. Moreover, the slope of 10-Cd-g-C$_3$N$_4$ was abated compared with g-C$_3$N$_4$, revealing that the electron donor density was increased in 10-Cd-g-C$_3$N$_4$. Owing to the higher electron donor density, the electrical conductivity and the mobility of charge carriers were increased, which helped for improving photocatalytic performance (Jun et al. 2013; Pan et al. 2018; Yang et al. 2013; Yuan et al. 2018; Zhou et al. 2014; Zhou et al. 2014). As estimated by the horizontal axis intercept, the flat band potential of g-C$_3$N$_4$ and 10-Cd-g-C$_3$N$_4$ were -0.84 eV and − 1.02 eV vs Ag/AgCl electrodes, respectively, which were tantamount to − 0.64 eV and − 0.82 eV vs normal hydrogen electrode (NHE), respectively. Commonly, conduction band potential (E$_{CB}$) is equivalent to flat band potential for an n-type semiconductor. As a consequence, the conduction band potential of g-C$_3$N$_4$ and 10-Cd-g-C$_3$N$_4$ were − 0.64 eV and − 0.82 eV vs NHE, respectively. And the valence band potential (E$_{VB}$) could obtain from the following equation (Zhang et al. 2010):

$$E_{VB} = E_{CB} + E_g$$

The E$_{VB}$ and E$_{CB}$ positions of as-prepared samples are revealed in Fig. S4. For g-C$_3$N$_4$, the E$_{CB}$ was -0.64 eV, on the basis of the experimental E$_g$ (2.57 eV), the E$_{VB}$ was 1.93 eV. For 10-Cd-g-C$_3$N$_4$, the E$_{CB}$ was − 0.82 eV, according to the experimental E$_g$ (2.29 eV), the E$_{VB}$ of 10-Cd-g-C$_3$N$_4$ was 1.47 eV.

The separation, transfer, and recombination of photogenerated carriers were analyzed by PL (Fig. 5d). Commonly, the weakened PL intensity meant enhanced separation and transfer efficiency of photogenerated carriers. For g-C$_3$N$_4$, the fluorescence emission peak appeared at 460 nm, which was consistent with the absorption threshold. Moreover, the strong intensity of the peak indicated the severe recombination of the photogenerated electron-hole pair in the g-C$_3$N$_4$ sample (Yu et al. 2013). Apparently, the fluorescence emission peak was red-shifted to 490 nm in 10-Cd-g-C$_3$N$_4$, which was corresponded to the bandgap narrowing effect (Gu et al.

2018; Zou et al. 2019). The intensity of the peak was significantly fell in 10-Cd-g-C$_3$N$_4$, which illustrated that Cd doping restrained the recombination of photoinduced electron-hole pair and accelerated the interfacial charge migration. Additionally, the PL spectra of other samples with different cadmium contents were manifested in Fig. S5, and the intensity of peak was lowest in 10-Cd-g-C$_3$N$_4$ (Thomas et al. 2008).

Other photoelectrochemical techniques such as photocurrent response measurement and electrochemical impedance spectroscopy (EIS) were employed to investigate the separation and transfer efficiency of photogenerated carriers. The photocurrent responses of as-prepared samples are revealed in Fig. 5e; both g-C$_3$N$_4$ and 10-Cd-g-C$_3$N$_4$ exhibited outstanding photostability under successive on/off visible light irradiation cycles. Moreover, the photocurrent response density of 10-Cd-g-C$_3$N$_4$ was significantly increased compared with g-C$_3$N$_4$, indicating the introduction of Cd increased the conductivity of g-C$_3$N$_4$ and accelerated the separation of the electron-hole pair (Ren et al. 2017). The EIS of g-C$_3$N$_4$ and 10-Cd-g-C$_3$N$_4$ are depicted in Fig. 5f. Commonly, the smaller arc radius meant smaller transfer resistance, namely, the better separation and transfer efficiency of photogenerated carriers (Lu et al. 2017; Yang et al. 2002). Notably, the arc radius of 10-Cd-g-C$_3$N$_4$ was smaller than g-C$_3$N$_4$, which reflects that 10-Cd-g-C$_3$N$_4$ possessed a high-efficiency separation ability and interfacial charge transfer level of photogenerated carriers (Zhu et al. 2015).

Photocatalytic activities

In this paper, TC was selected as a contaminant. For testing the effect of Cd doping content on degradation performance, a series of comparative degradation experiments were carried out under the simulated visible light irradiation (λ > 420 nm). As illustrated in Fig. 6a, the degradation rate of TC can be neglected without catalysts, owing to the high stability of TC under visible light. Moreover, the adsorption capacity of all Cd-doped g-C$_3$N$_4$ samples was larger than that of g-C$_3$N$_4$, corresponding to the increase of specific surface area after Cd doping. All Cd-doped g-C$_3$N$_4$ samples exhibited great increased photocatalytic degradation performance after 60-min visible light irradiation compared with g-C$_3$N$_4$ (43.9%), confirming the doping of Cd was truly enhanced the photocatalytic efficiency (Abu Hanif et al. 2021).

At first, the degradation performance of TC was enhanced with the increase of Cd doping content. As the doping content of Cd increased, the utility efficiency of visible light was promoted; as a consequence, more photogenerated carriers were provided. The 10-Cd-g-C$_3$N$_4$ sample exhibited the highest photocatalytic degradation performance (98.1%). Unfortunately, when the doping content of Cd continuously increased, the degradation performance was decreased. The photocatalytic degradation performance of
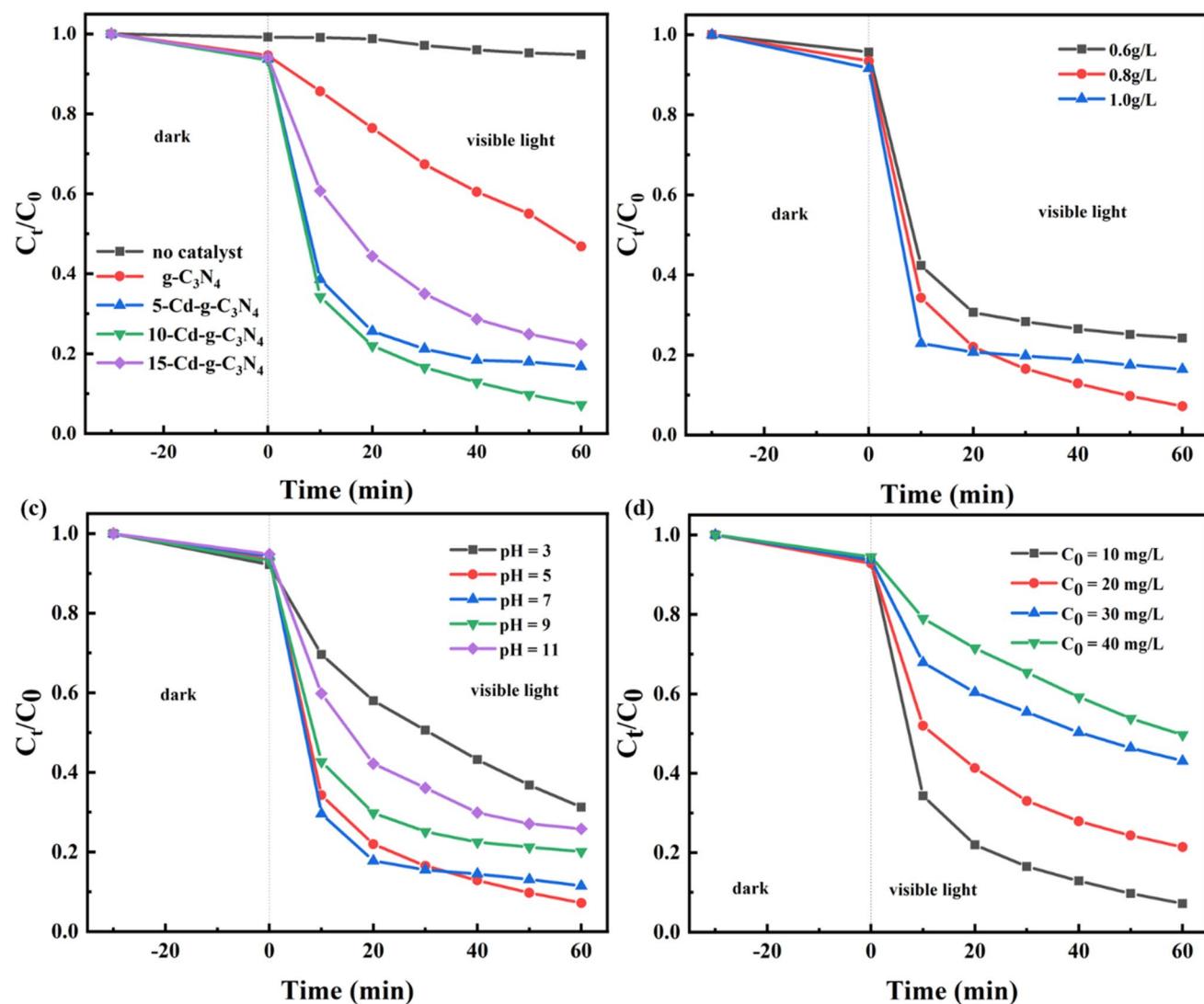
Fig. 6 a Degradation performance of catalysts curves with different amounts cadmium. Experimental conditions: $[Cd\text{-}g\text{-}C_3N_4]_0 = 0.8$ g L^{-1}, $[TC]_0 = 10$ mg L^{-1}, and T = 25 °C. **b** Degradation efficiency of different catalyst dosages. Experimental conditions: $[TC]_0 = 10$ mg L^{-1}, and T = 25 °C. **c** Degradation efficiency of 10-Cd-g-C_3N_4 composites with different pH. Experimental conditions: $[10\text{-}Cd\text{-}g\text{-}C_3N_4]_0 = 0.8$ g L^{-1}, $[TC]_0 = 10$ mg L^{-1}, and T = 25 °C. **d** Degradation efficiency of catalyst with different initial TC concentrations. Experimental conditions: $[10\text{-}Cd\text{-}g\text{-}C_3N_4]_0 = 0.8$ g L^{-1}, and T = 25 °C.

the 15-Cd-g-C_3N_4 sample was only 75.9%, indicating the excessive Cd element could serve as the recombination center of the photogenerated carrier or block the surface active sites, as a result restraining the light absorption capacity and inhibiting photocatalytic degradation performance (Li et al. 2009a; Zhang et al. 2016b; Zhang et al. 2010).

The degradation reaction kinetic of as-prepared catalysts was further investigated by the pseudo-first-order kinetic model, and the formula was expressed as follows:

$$\ln \left(C_t/C_0 \right) = -K_{app}t$$

where C_0 is the initial concentration of TC, C_t is the concentration of TC at time t, and K_{app} is the reaction rate constant (min^{-1}). The pseudo-first-order kinetic plots of as-prepared catalysts are presented in Fig. S6. Results indicated the K_{app} of Cd-g-C_3N_4 samples was higher than g-C_3N_4, and the K_{app} of 10-Cd-g-C_3N_4 sample was the highest, demonstrating that 10-Cd-g-C_3N_4 had the best photocatalytic performance.

Additionally, the photocatalytic degradation performance within 10 min of the 10-Cd-g-C_3N_4 sample was also tested (Fig. S7). The result illustrated that the TC was degraded by almost 80% within 10 min. Table S4 illustrates the comparison with other similar types of research, and we found

the removal rate of this work was excellent by comparing it with other similar types of work.

The effects of different reaction conditions, such as initial concentration of TC, catalyst dosage, and pH of solution, were studied to meet the practical application. Figure 6b displays the effect of catalyst dosages on TC photodegradation. As the catalyst dosages increased from 0.6 g/L to 0.8 g/L, the degradation rate of TC was enhanced monotonically, which could ascribe to the increased surface active sites, leading to more TC absorbed on the surface of materials. The catalyst dosages at 0.8 g/L displayed the best photocatalytic degradation performance. Nevertheless, with further adding the catalyst dosages to 1.0 g/L, the degradation rate of TC was decreased slightly, which owing to the excessive catalyst could reduce the photo-adsorption ability, hindering the effective migration of photogenerated carriers (Zhang et al. 2016a).

For testing the effect of solution pH on degradation performance, diluted hydrochloric acid and sodium hydroxide were used to adjust the initial pH of the solution. As clarified in Fig. 6c, with the initial pH decreasing from 11 to 5, the degradation rate of TC was enhanced monotonically. The initial pH of the solution at 5 exhibited the best degradation efficiency of TC (94.4%), which can be explained by the surface charge of TC and materials. Additionally, with further decreasing the initial pH to 3, the degradation rate of TC was decreased significantly, which could ascribe to the decomposition of catalyst in strongly acidic conditions.

The effect of the initial concentration of TC on degradation performance was illuminated in Fig. 6d. It could be notably detected that the removal rates were abated with the initial concentration increased, and the best removal rate was 96.7% at the initial concentration of 10 mg/L. Two possible reasons could be proposed to elucidate this tendency. Firstly, high concentrations of contaminants might accumulate at the surface of the catalyst, inhibiting the light absorption capacity. Secondly, intermediate products produced in the process of contaminants degradation might occupy the surface active site, leading to no contact between contaminants and the catalyst.

To study the effect of the water matrix on degradation performance, we used the as-prepared catalyst to set up a control test in actual water. Four different water matrices were chosen, such as ultra-pure water, tap water, lake water (Houhu, Changsha), and river water (Xiangjiang, Changsha). The basic parameter information of these four types of water is listed in Table S4. As clarified in Fig. 7a, obviously, the degradation rate of TC was the highest in ultra-pure water, while the degradation rate of TC was inhibited in the other three types of water. The degradation rate of TC was 81.8% in tap water, the degradation rate was 82.2% in lake water, and that was 71.1% in river water. Thus, the reason for the degradation rate of TC decreased could be

the different content and composition of inorganic anions and organic matter in actual water. Moreover, the first-order plots of the effect of the water matrix are analyzed in Fig. 7b.

In order to evaluate the practicability of catalysts, the stability tests were carried out on the degradation experiment by reusing the catalyst. Figure 7c depicts the degradation rates of TC in four consecutive cycles. Obviously, the degradation rates of TC were slightly decreased with the increase of reuse time of 10-Cd-g-C_3N_4, which could attribute to the catalyst loss during the collection process. The degradation rates of TC still maintained a high level (89.5%) in the fourth cycle. Moreover, the XRD was also carried out to demonstrate the difference between catalysts before and after use (Fig. 7d). No obvious peak changes were found in the used catalyst, indicating the outstanding stability of 10-Cd-g-C_3N_4.

The ability of mineralization is an important index to ascertain the degree of contaminants removal in the photocatalytic process. As intriguingly indicated in Fig. S8, the mineralization efficiency of TC reached 34% within 60 min under visible light irradiation, which confirmed that 10-Cd-g-C_3N_4 could degrade TC into small-molecule intermediate compounds (CO_2, H_2O).

Degradation pathway and mechanism

The trapping experiments were carried out on degradation experiments to determine the active species participating in the degradation process (Li et al. 2015). EDTA-2Na, IPA, and TEMPO were added to the solution as scavengers to capture h^+, •OH, and •O_2^-, respectively. As illustrated in Fig. 8a–b, the degradation rate of TC was largely suppressed by EDTA-2Na, indicating that h^+ was the dominant active species in the degradation process. Similarly, the degradation rate of TC was inhibited slightly with the addition of TEMPO and IPA, revealing that •O_2^- and •OH played auxiliary roles in the photocatalytic degradation process (Yan et al. 2010; Yu et al. 2018).

The above results were further verified by ESR, in which the DMPO was used as scavengers to capture •OH and •O_2^-. As illustrated in Fig. 8c and Fig. 8d, it is hard to see the up and down signals of active species (neither •OH nor •O_2^-) under dark conditions. Notably, the four-strong intensity signals could be found under the visible light irradiation, the intensity ratio of 1:2:2:1 were corresponded to •OH radical, and the intensity ratio of 1:1:1:1were corresponded to •O_2^- radical, proving the visible light is prerequisite for 10-Cd-g-C_3N_4 to product •OH and •O_2^- active species.

For an in-depth understanding of the photocatalytic degradation mechanism in the presence of the 10-Cd-g-C_3N_4 catalyst, liquid chromatograph-mass spectrometer (LC-MS) techniques were carried out to precisely identify the intermediates of TC during the photocatalytic degradation
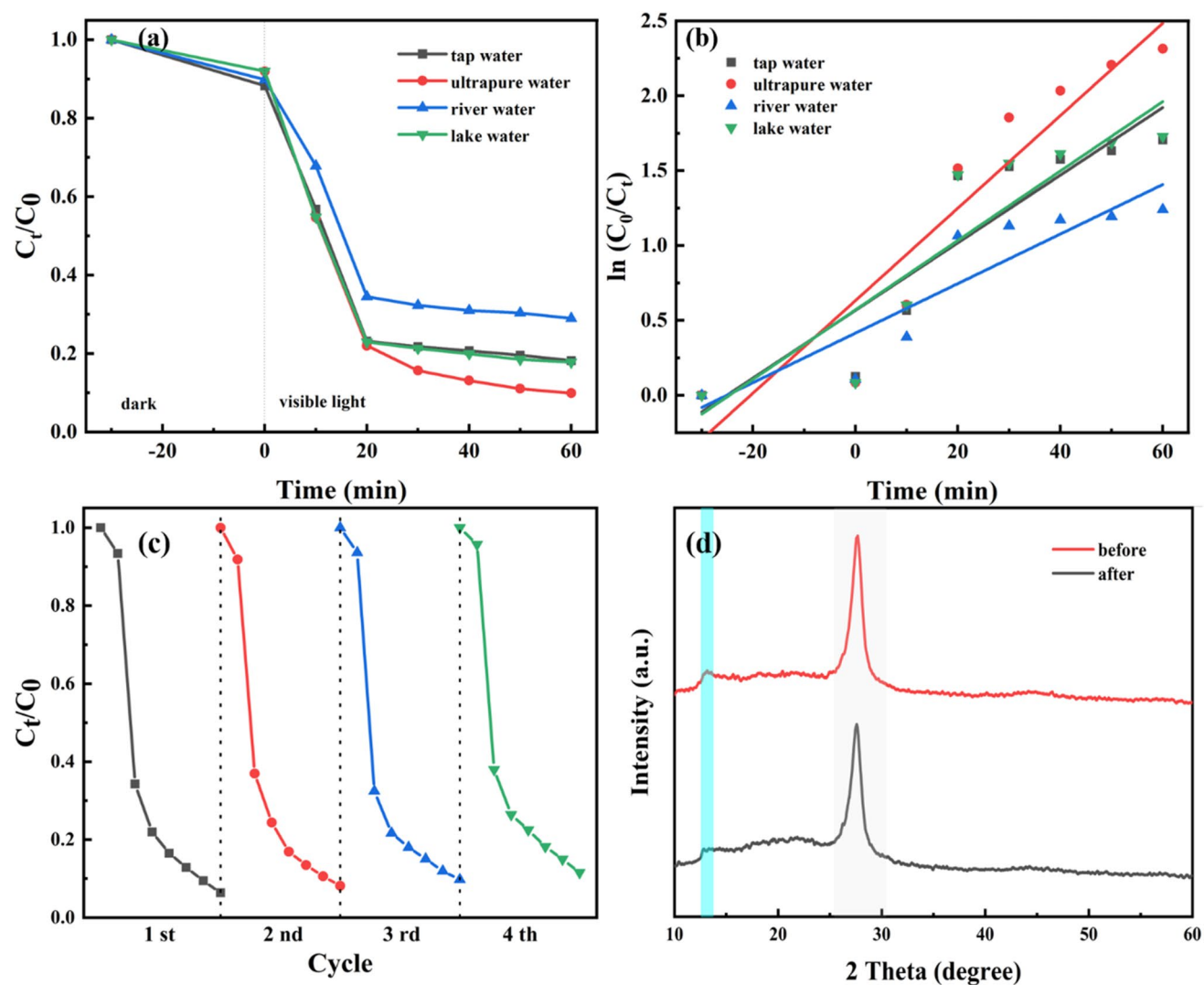
Fig. 7 **a** Degradation performance of catalysts curves with different water matrix. **b** First-order plots of photocatalytic degradation with different water matrix. Experimental conditions: $[Cd\text{-}g\text{-}C_3N_4]_0 = 0.8$ g L^{-1}, $[TC]_0 = 10$ mg L^{-1}, and T = 25 °C. **c** Degradation efficiency of TC over 10-Cd-g-C_3N_4 photocatalyst under four cycling tests. **d** XRD images of 10-Cd-g-C_3N_4 photocatalyst before and after four times used. Experiments conditions: TC concentration = 20 mg/L; catalyst loading = 0.8 g/L, Temperature = 25 °C

process. The LC-MS chromatogram of the TC degradation process under visible light irradiation is shown in Fig. S9. Clearly, with the progress of the reaction process, the peak of TC (m/z = 445) was faded away. Several newly appeared peaks corresponded to the reactive intermediates that were produced during the photocatalytic degradation process. Moreover, the mass spectrum of the TC degradation process provided a piece of important information for possible molecular structures of intermediates, in which the charge-to-mass ratio (m/z) of intermediates was clearly detected (Fig. 9). According to the listed m/z of intermediates, the possible degradation process of TC was proposed (Fig. 10). Firstly, one methyl in the amino group of TC was attacked by •OH to generate hydroxylated product P1 (m/z = 475). In another pathway, P2 (m/z = 429) was formed by the

dehydration of TC. Subsequently, P3 (m/z = 385) intermediate was produced through the N-demethylation and deamination process of P2, and P3 was undergo the cleavage of carbon atomic ring and double-bond fracture, as a result of generating P4 (m/z = 341). Then, the further loss of ketone and aldehyde of P4 led to the generation of P5 (m/z =221). In another pathway, the ring-opening process of P3 was occur, which caused the formation of P6 (m/z = 301). P6 was attacked by the •OH to generate hydroxylated product P7 (m/z = 285). Then, the P8 (m/z = 235) was produced through the decarboxylation of P7. Moreover, the P8 could also change to P5 through the hydrogenation and double-bond fracture, and the formation of P9 (m/z = 149) was through the further ring-opening reaction of P8. In addition, the P10 (m/z = 141) was generated by demethylation and
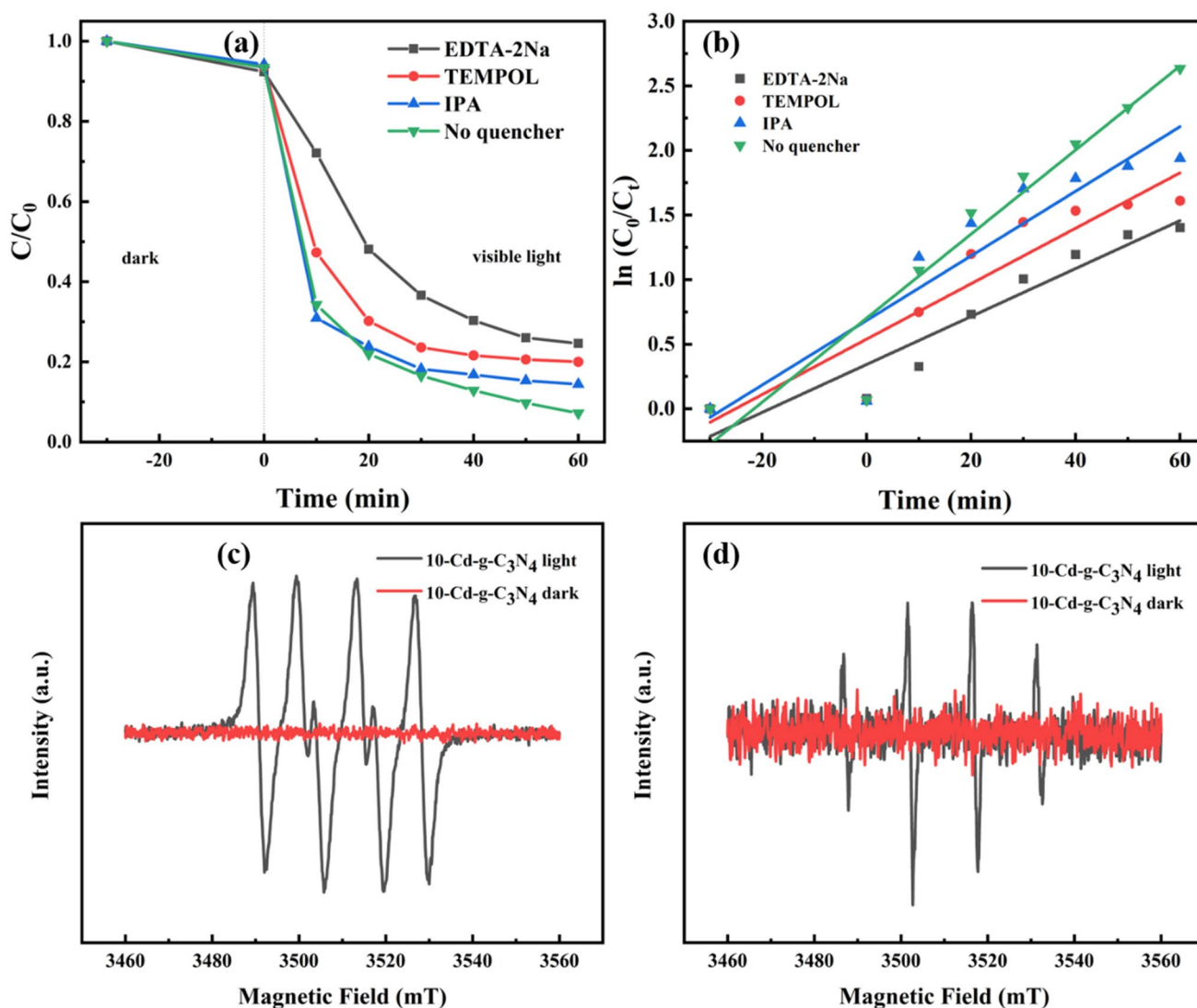
Fig. 8 **a** Degradation efficiency of 10-Cd-g-C₃N₄ photocatalyst under different quenchers. **b** First-order plots of photocatalytic degradation under different quenchers. Experiment conditions: TC concentration = 20 mg/L; catalyst loading = 0.8 g/L, temperature = 25 °C. ESR spectra for **c** DMPO⁻ •O₂⁻and **d** DMPO⁻ •OH under dark and visible light condition

losing the ketone of P8. Finally, with further deamidation, losing ketone and aldehyde, dihydroxylation, ring-opening reaction, successive detachment of branched-chain groups, and double-bond fracture, the intermediates were completely decomposed into CO_2, H_2O, or other small molecules.

Due to the heavy metal properties of cadmium, it is necessary to carry out the ion leaching experiments on the solution after the reaction. Experimental data (Fig. S10) showed that the cadmium ion leaching rate was far less than 0.1 mg/L, which was prescribed by the national integrated wastewater discharge Standard of the People's Republic of China (GB 8978–1996). At the same time, by comparing the leaching rate of the catalyst without oil bath treatment and that of the catalyst with oil bath treatment, we found that the leaching rate of the catalyst with oil bath treatment was far less than that of the catalyst without oil bath treatment, indicating that the oil bath pre-treatment made the combination of cadmium and carbon nitride closer. The cadmium leaching in the four cycles was 3.818 ug/L, 3.519 ug/L, 3.230 ug/L, and 3.093 ug/L, respectively. Due to the leaching of cadmium, the doping rate between Cd and g-C₃N₄ was decreased, which corresponded to the decreased degradation rate of TC in the cycle experiments.

According to all aforementioned results, the introduction of Cd accelerated the separation and transfer rate of electron-hole pairs, decreasing the recombination rate of photogenerated carriers, and providing more reactive active sites, thus enhancing the photocatalytic degradation property. A brief mechanism of the 10-Cd-g-C₃N₄ sample during the TC degradation process is summarized
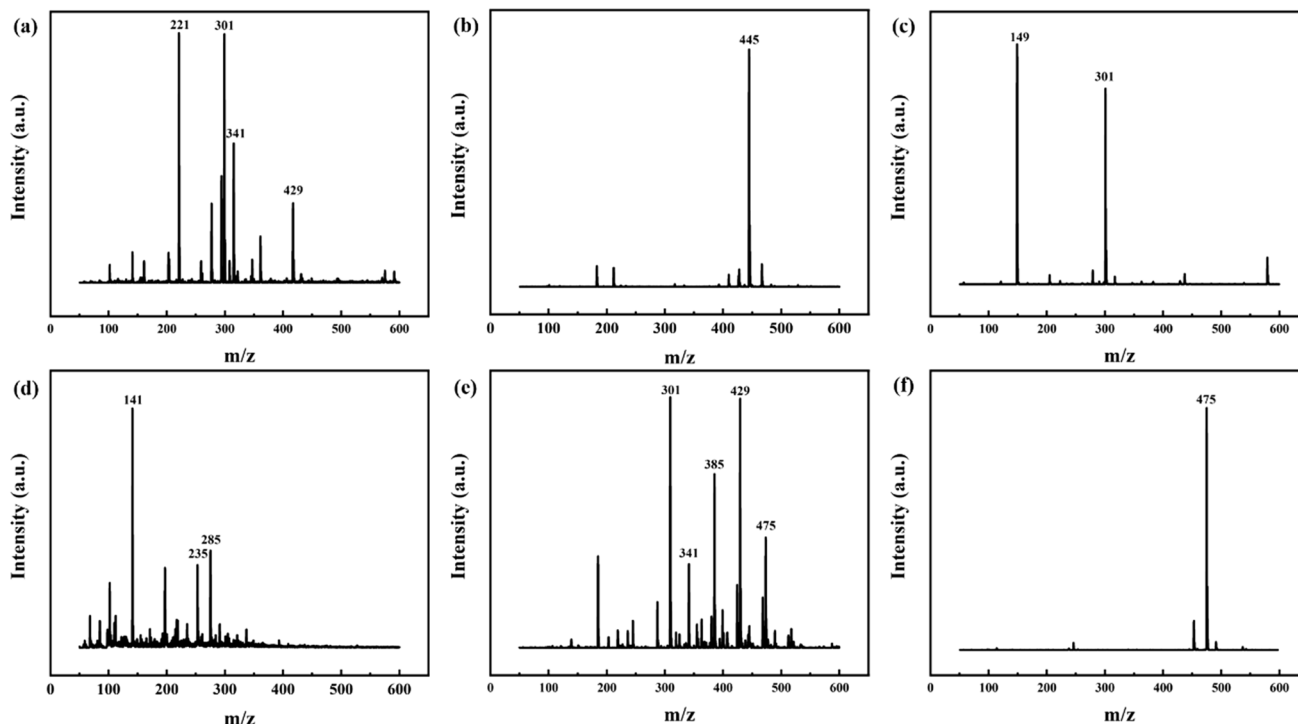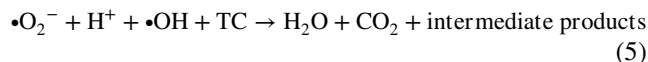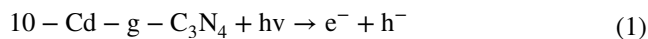
Fig. 9 The mass spectrum of possible intermediates produced during the photocatalytic degradation process

in Scheme 1. First, the photogenerated electron-hole pairs were generated under visible light irradiation, and the photogenerated electron-hole pairs were separated spontaneously. Furthermore, the electrons were transferred to the conduction band, as a consequence, leaving holes at the valence band (Eq. (1)), the accumulated holes at the valence band could direct react with TC. Then, the O_2 absorbed at the catalyst surface could react with electrons accumulated at the conduction band to form superoxide radical (Eq. (2)), owing to the E_{CB} of 10-Cd-g-C_3N_4 (-0.82 eV vs NHE) being negative than $O_2/\bullet O_2^-$ (− 0.33 eV vs NHE). The surplus electrons at the conduction band could further react with superoxide radicals to form hydrogen peroxide (Eq. (3)). However, the holes accumulated at the valence band could not react with OH^- to form •OH because the E_{VB} of 10-Cd-g-C_3N_4 (1.47 eV vs NHE) was negative than $OH^-/\bullet OH$ (2.40 eV vs NHE), which was not consistent with the result of trapping experiments and ESR. Consequently, the •OH probably derived from another way like H_2O_2 decomposition (Eq. (4)) (Jia et al. 2020), the evolution of H_2O_2 was detected by iodometry (Fig. S11), in which the evolution of H_2O_2 was increased with the irradiation time. Finally, h^+, $\bullet O_2^-$ and •OH were worked together to degrade TC into small molecules (Eq. (5)). The reaction equations involved in the photocatalytic reaction process were manifested below.

$$10 - Cd - g - C_3N_4 + hv \rightarrow e^- + h^- \tag{1}$$

$$O_2 + e^- \rightarrow \bullet O_2^- \tag{2}$$

$$\bullet O_2^- + e^- + 2H^+ \rightarrow H_2O_2 \tag{3}$$

$$H_2O_2 + e^- \rightarrow \bullet OH + OH^- \tag{4}$$

$$\bullet O_2^- + H^+ + \bullet OH + TC \rightarrow H_2O + CO_2 + intermediate\ products \tag{5}$$

Conclusion

In summary, the commendable 10-Cd-g-C_3N_4 photocatalyst was successfully prepared via the thermal polymerization method after the oil bath pretreat. The degradation experiments demonstrated explicitly that the photocatalytic activity of g-C_3N_4 could be enhanced significantly with the doping of Cd. Under an hour of visible light irradiation, the removal efficiency of 10-Cd-g-C_3N_4 (98.1%) was 2.0 times enhanced in comparison with g-C_3N_4 (43.9%). Based on the characterization analysis,
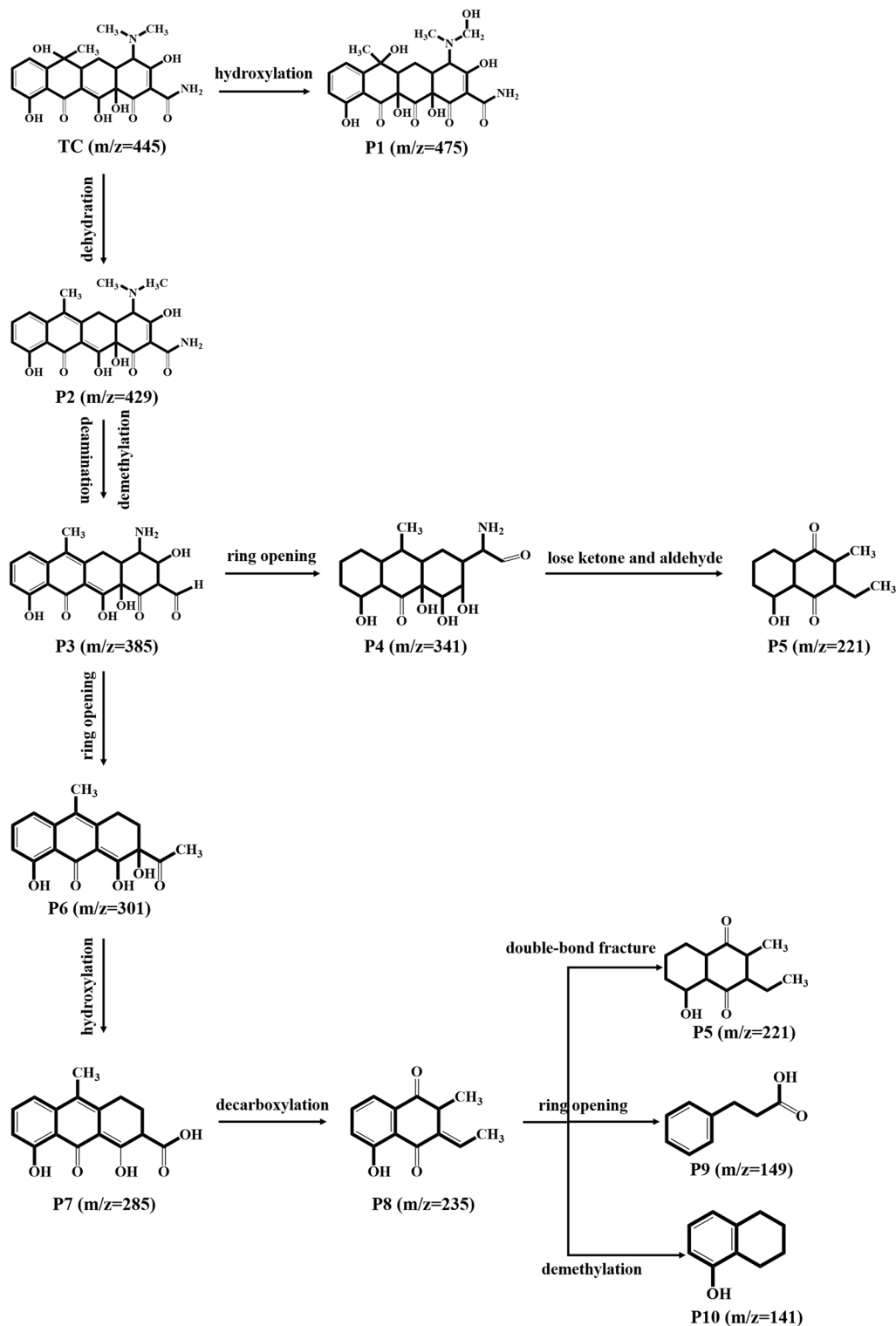
Fig. 10 The possible degradation pathway of TC molecule during the degradation process

the enhanced photocatalytic performance by Cd doping could ascribe to the following reasons: firstly, the enhanced photo-absorption ability, accelerating the migration, separation, and transfer efficiency of photogenerated carriers. Meanwhile, Cd doping adjusted the potential of CB and VB of g-C_3N_4 to prolong the photo-absorption ability. Finally, the ultrathin mesoporous structure and the increased surface area could provide more active sites

Scheme 1 The transfer and separation of charges and degradation mechanisms in the 10-Cd-g-C_3N_4 under visible-light irradiation
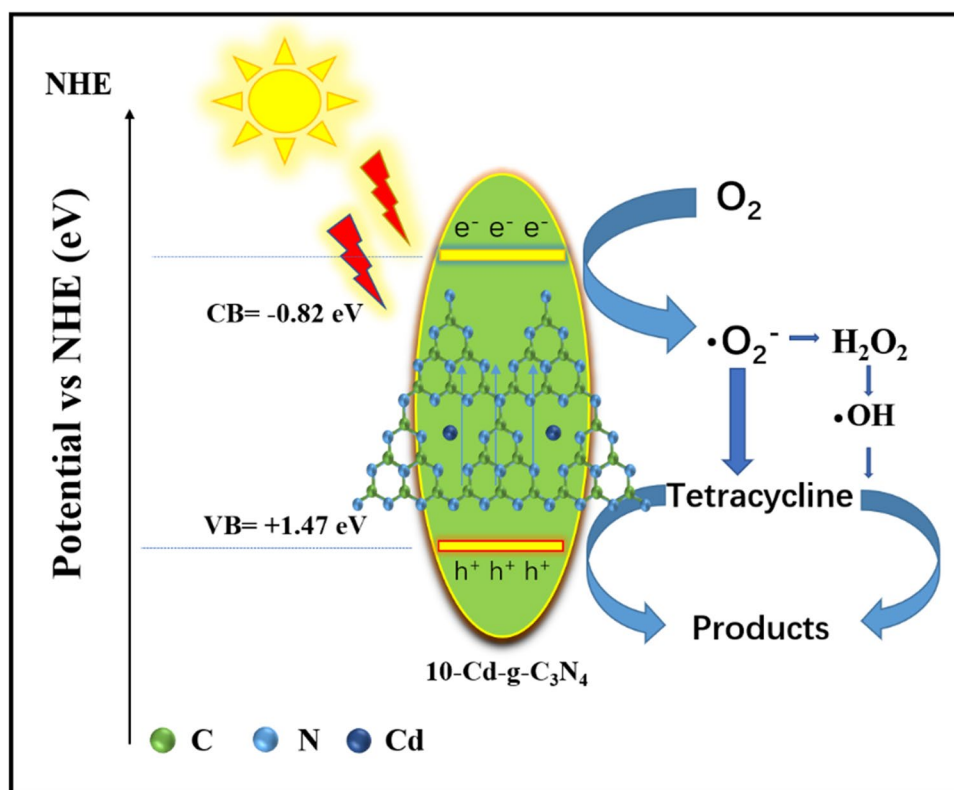
along with a shortened electron-transfer pathway, which was conducive to inhibiting the recombination of the photogenerated electrons and holes.

Data availability All data generated or analyzed during the current study are included in this article and its supplementary information files.

Author contribution YZ: Responsible for writing papers, conducting experiments, drawing the chart, and analyzing the characterization part. HQ, ZW, HW, YH, QT, QL, PX: Responsible for reviewing the article and providing suggestions for revisions. The first draft of the manuscript was written by YZ and all authors commented on previous versions of the manuscript. All authors read and approved the final manuscript.

Declarations

Ethics approval Not applicable.

Consent to participate Not applicable.

Consent to publish Not applicable.

Competing interests The authors declare no competing interests.

References

Abbott D (2010) Keeping the energy debate clean: how do we supply the world's energy needs? Proc IEEE 98:42–66. https://doi.org/10.1109/jproc.2009.2035162

Abu Hanif M, Akter J, Akherul Islam M, Sapkota KP, Hahn JR (2021) Visible-light-driven enhanced photocatalytic performance using cadmium-doping of tungsten (VI) oxide and nanocomposite formation with graphitic carbon nitride disks. Appl Surf Sci 565:150541. https://doi.org/10.1016/j.apsusc.2021.150541

Amirthaganesan G, Dhanabal T, Nanthini K, Dhandapani M (2010) Thermal and FTIR spectral characterization of diammonium tetrachloromanganate (II) monohydrate crystals. Mater Lett Mater Lett 64:264–266. https://doi.org/10.1016/j.matlet.2009.10.057

Butchosa C, Guiglion P, Zwijnenburg MA (2014) Carbon nitride photocatalysts for water splitting: a computational perspective. J Phys Chem C 118:24833–24842. https://doi.org/10.1021/jp507372n

Chan D, Yu J, Yecheng L, Hu Z (2017) A metal-free composite photocatalyst of graphene quantum dots deposited on red phosphorus. J Environ Sci 60:91–97. https://doi.org/10.1016/j.jes.2016.11.025

Chang F, Li C, Luo J, Xie Y, Deng B, Hu X (2015) Enhanced visible-light-driven photocatalytic performance of porous graphitic carbon nitride. Appl Surf Sci 358:270–277. https://doi.org/10.1016/j.apsusc.2015.08.124

Chang F, Yan W, Cheng W, Wu F, Deng B, Hu X (2018) The construction and enhanced photocatalytic performance of binary

composite S/g-C$_3$N$_4$. Mater. Sci. Semicond. Process 87:1–6. https://doi.org/10.1016/j.mssp.2018.07.005

Chao K, Liao H, Shyue J, Lian S-S (2014) corrosion behavior of high nitrogen nickel-free Fe-16Cr-Mn-Mo-N stainless steels. Metall Mater Trans B 45:381–391. https://doi.org/10.1007/s11663-013-9891-z

Chen X, Peng X, Jiang L, Yuan X-Z, Yu H, Hou W, Zhang J, Xia Q (2020) Recent advances in titanium metal-organic frameworks and their derived materials: features, fabrication, and photocatalytic applications. Chem Eng J 395:125080. https://doi.org/10.1016/j.cej.2020.125080

Chen Q, Wan B, Zhu P, Xu S, Huang Y (2021) The synergy of adsorption and photosensitization of platinum-doped graphitic carbon nitride for improved removal of rhodamine B. Environ Sci Pollut Res: DOI: https://doi.org/10.1007/s11356-021-15340-0

Chou S-Y, Chen C-C, Dai Y-M, Lin J-H, Lee WW (2016) Novel synthesis of bismuth oxyiodide/graphitic carbon nitride nanocomposites with enhanced visible-light photocatalytic activity. RSC Advances 6:33478–33491. https://doi.org/10.1039/c5ra28024a

Fan J, Qin H, Jiang S (2019) Mn-doped g-C$_3$N$_4$ composite to activate peroxymonosulfate for acetaminophen degradation: the role of superoxide anion and singlet oxygen. Chem Eng J 359:723–732. https://doi.org/10.1016/j.cej.2018.11.165

Fang LJ, Wang XL, Zhao JJ, Li YH, Wang YL, Du XL, He ZF, Zeng HD, Yang HG (2016) One-step fabrication of porous oxygen-doped g-C$_3$N$_4$ with feeble nitrogen vacancies for enhanced photocatalytic performance. Chem Commun 52:14408–14411. https://doi.org/10.1039/c6cc08187h

Gao J, Zhou Y, Li Z, Yan S, Wang N, Zou Z (2012) High-yield synthesis of millimetre-long, semiconducting carbon nitride nanotubes with intense photoluminescence emission and reproducible photoconductivity. Nanoscale 4:3687–3692. https://doi.org/10.1039/c2nr30777d

Gao H, Yan S, Wang J, Huang YA, Wang P, Li Z, Zou Z (2013) Towards efficient solar hydrogen production by intercalated carbon nitride photocatalyst. Phys Chem Chem Phys 15:18077–18084. https://doi.org/10.1039/c3cp53774a

Ge L, Han C, Liu J, Li Y (2011) Enhanced visible light photocatalytic activity of novel polymeric g-C$_3$N$_4$ loaded with Ag nanoparticles. Appl Catal A: Gen 409-410:215–222. https://doi.org/10.1016/j.apcata.2011.10.006

Ge L, Zuo F, Liu J, Ma Q, Wang C, Sun D, Bartels L, Feng P (2012) Synthesis and efficient visible light photocatalytic hydrogen evolution of polymeric g-C$_3$N$_4$ coupled with CdS quantum dots. J Phys ChemC 116:13708–13714. https://doi.org/10.1021/jp3041692

Gu Y, Yu Y, Zou J, Shen T, Xu Q, Yue X, Meng J, Wang J (2018) The ultra-rapid synthesis of rGO/g-C$_3$N$_4$ composite via microwave heating with enhanced photocatalytic performance. Mater Lett 232:107–109. https://doi.org/10.1016/j.matlet.2018.08.077

Huang D, Chen S, Zeng G, Gong X, Zhou C, Cheng M, Xue W, Yan X, Li J (2019) Artificial Z-scheme photocatalytic system: what have been done and where to go? Coor Chem Rev 385:44–80. https://doi.org/10.1016/j.ccr.2018.12.013

Iqbal W, Dong C, Xing M, Tan X, Zhang J (2017) Eco-friendly one-pot synthesis of well-adorned mesoporous g-C$_3$N$_4$ with efficiently enhanced visible light photocatalytic activity. Catal. Sci. Technol. 7:1726–1734. https://doi.org/10.1039/c7cy00286f

Ji C, Du C, Steinkruger JD, Zhou C, Yang S (2019) In-situ hydrothermal fabrication of CdS/g-C$_3$N$_4$ nanocomposites for enhanced photocatalytic water splitting. Mater Lett 240:128–131. https://doi.org/10.1016/j.matlet.2018.12.128

Jia J, Jiang C, Zhang X, Li P, Xiong J, Zhang Z, Wu T, Wang Y (2019) Urea-modified carbon quantum dots as electron mediator decorated g-C$_3$N$_4$/WO$_3$ with enhanced visible-light photocatalytic activity and mechanism insight. Appl Surf Sci 495:143524. https://doi.org/10.1016/j.apsusc.2019.07.266

Jia J, Zhang X, Jiang C, Huang W, Wang Y (2020) Visible-light-driven nitrogen-doped carbon quantum dots decorated g-C$_3$N$_4$/Bi$_2$WO$_6$ Z-scheme composite with enhanced photocatalytic activity and mechanism insight. J All Com 835:155180. https://doi.org/10.1016/j.jallcom.2020.155180

Jun Y-S, Lee E, Wang X, Hong W, Stucky G, Thomas A (2013) From melamine-cyanuric acid supramolecular aggregates to carbon nitride hollow spheres. Adv Funct Mater 23(29):3661–3667. https://doi.org/10.1002/adfm.201203732

Katsumata H, Sakai T, Suzuki T, Knaeco S (2014) Highly efficient photocatalytic activity of g-C$_3$N$_4$/Ag$_3$PO$_4$ hybrid photocatalysts through Z-scheme photocatalytic mechanism under visible light. Ind. Eng. Chem. Res. 53:8018–8025. https://doi.org/10.1021/ie5012036

Kong L, Yujin J, Dang Z, Yan J, Li P, Li Y (2018) g-C$_3$N$_4$ Loading black phosphorus quantum dot for efficient and stable photocatalytic H$_2$ generation under visible light. Adv Funct Mater 28:1800668. https://doi.org/10.1002/adfm.201800668

Li J, Xu J, Dai W-L, Li H, Fan K (2009a) Direct hydro-alcohol thermal synthesis of special core–shell structured Fe-doped titania microspheres with extended visible light response and enhanced photoactivity. Appl Catal B: Environ 85:162–170. https://doi.org/10.1016/j.apcatb.2008.07.008

Li X, Zhang J, Shen L, Yanmei M, Lei W, Cui Q, Zou G (2009b) Preparation and characterization of graphitic carbon nitride through pyrolysis of melamine. Appl Phys A 94:387–392. https://doi.org/10.1007/s00339-008-4816-4

Li H, Liu Y, Gao X, Fu C, Wang X (2015) Facile synthesis and enhanced visible-light photocatalysis of graphitic carbon nitride composite semiconductors. ChemSusChem 8(7):1189–1196. https://doi.org/10.1016/j.cattod.2017.05.017

Li Z, Liu Z, Li B, Li D, Ge C, Fang Y (2016) Novel CdS nanorods/g-C$_3$N$_4$ nanosheets 1-D/2-D hybrid architectures: an in situ growth route and excellent visible light photoelectrochemical performances. J Mater Sci Mater Elect 27:2904–2913. https://doi.org/10.1007/s10854-015-4108-7

Li H, Shan C, Pan B (2018) Fe(III)-Doped g-C$_3$N$_4$ Mediated peroxymonosulfate activation for selective degradation of phenolic compounds via high-valent iron-oxo species. Environ Sci Technol 52:2197–2205. https://doi.org/10.1021/acs.est.7b05563

Liu G, Niu P, Smith S, Chen Z-G, Lu M, Cheng H-M (2010) Unique electronic structure induced high photoreactivity of sulfur-doped graphitic C$_3$N$_4$. J Am Chem Soc 132:11642–11648. https://doi.org/10.1021/ja103798k

Liu W, Wang M, Xu C, Chen S (2012) Facile synthesis of g-C$_3$N$_4$/ZnO composite with enhanced visible light photooxidation and photoreduction properties. Chem Eng J 209:386–393. https://doi.org/10.1016/j.cej.2012.08.033

Liu J, Liu Y, Naiyun L, Han Y, Zhang X, Huang H, Lifshitz Y, Lee S-T, Zhong J, Kang ZH (2015) ChemInform Abstract: metal-free efficient photocatalyst for stable visible water splitting via a two-electron pathway. Science (New York, N.Y.) 347: 970-4. DOI: https://doi.org/10.1126/science.aaa3145

Liu S, Li D, Sun H, Ang HM, Tadé MO, Wang S (2016) Oxygen functional groups in graphitic carbon nitride for enhanced photocatalysis. J Coll Inter Sci 468:176–182. https://doi.org/10.1016/j.jcis.2016.01.051

Liu Y, He M, Guo R, Fang Z, Kang S, Ma Z, Dong M, Wang W, Cui L (2020) Ultrastable metal-free near-infrared-driven photocatalysts for H$_2$ production based on protonated 2D g-C$_3$N$_4$ sensitized with Chlorine6. Appl Catal B: Environ 260:118137. https://doi.org/10.1016/j.apcatb.2019.118137

Lu Q, Deng J, Hou Y, Wang H, Li H, Zhang Y (2015) One-step electrochemical synthesis of ultrathin graphitic carbon nitride

nanosheets and their application to the detection of uric acid. Chem Commun 51:12251–12253. https://doi.org/10.1039/c5cc04231c

Lu Z, Song W, Ouyang C, Wang H, Zeng D, Xie C (2017) Enhanced visible-light photocatalytic performance of highly-dispersed Pt/g-C₃N₄ nanocomposites by one-step solvothermal treatment. RSC Adv. 7:33552–33557. https://doi.org/10.1039/c7ra04931e

Luo L, Zhang A, Janik MJ, Li K, Song C, Guo X (2017) Facile fabrication of ordered mesoporous graphitic carbon nitride for RhB photocatalytic degradation. Appl Surf Sci 396:78–84. https://doi.org/10.1016/j.apsusc.2016.10.190

Matanović I, Babanova S, Iii A, Serov A, Artyushkova K, Atanassov P (2015) Bio-inspired design of electrocatalysts for oxalate oxidation: a combined experimental and computational study of Mn-N-C catalyst. Phys. Chem. Chem. Phys. 17:13235–13244. https://doi.org/10.1039/c5cp00676g

McCauley S, Stephens J (2012) Green energy clusters and sociotechnical transitions: Analysis of a sustainable energy cluster for regional economic development in Central Massachusetts, USA. Sustain Sci 7:213–225. https://doi.org/10.1007/s11625-012-0164-6

Narkbuakaew T, Sujaridworakun P (2020) Synthesis of Tri-S-Triazine Based g-C₃N₄ Photocatalyst for Cationic Rhodamine B Degradation under Visible Light. Top. Catal. 63:1086–1096. https://doi.org/10.1007/s11244-020-01375-z

Ong W-J, Tan L-L, Ng YH, Yong S-T, Chai S-P (2016) Graphitic CARBON NITRIDE (g-C₃N₄)-based photocatalysts for artificial photosynthesis and environmental remediation: are we a step closer to achieving sustainability? Chem Rev 116:7159–7329. https://doi.org/10.1021/acs.chemrev.6b00075

Ou M, Zhong Q, Zhang S, Yu L (2015) Ultrasound assisted synthesis of heterogeneous g-C₃N₄/BiVO₄ composites and their visible-light-induced photocatalytic oxidation of NO in gas phase. J All Com 626:401–409. https://doi.org/10.1016/j.jallcom.2014.11.148

Pan J, Feng S, Zhao C, Dong Z, Wang B, Wang J, Song C, Zheng Y, Li C (2018) The enhanced photocatalytic hydrogen production of the fusiform g-C₃N₄ modification CaTiO₃ nano-heterojunction. Intl J Hyd Energy 43(14):19019–19028. https://doi.org/10.1016/j.ijhydene.2018.08.102

Park S-S, Chu S-W, Xue C, Zhao D, Ha C-S (2011) Facile synthesis of mesoporous carbon nitrides using the incipient wetness method and the application as hydrogen adsorbent. J. Mater. Chem. 21:10801–10807. https://doi.org/10.1039/c7ra02178j

Qi Y, Liang Q, Lv R, Shen W, Kang F, Huang Z-H (2018) Synthesis and photocatalytic activity of mesoporous g-C₃N₄/MoS₂ hybrid catalysts. R Soc Open Sci 5:180187–180187. https://doi.org/10.1098/rsos.180187

Reddy NR, Reddy PM, Mandal TK, Yedluri AK, Joo SW (2021) Architecture of superior hybrid electrode by the composition of Cu₂O nanoflakes, novel cadmium ferrite (CdFe₂O₄) nanoparticles, and g-C₃N₄ sheets for symmetric and asymmetric supercapacitors. J Energy Stor 43:103302. https://doi.org/10.1016/j.est.2021.103302

Ren K, Yin P, Zhou Y, Cao X, Dong C, Cui L, Liu H, Du X (2017) Localized defects on copper sulfide surface for enhanced plasmon resonance and water splitting. Small 13:1700867. https://doi.org/10.1002/smll.201700867

Schwinghammer K, Mesch M, Duppel V, Ziegler C, Senker J, Lotsch B (2014) Crystalline carbon nitride nanosheets for improved visible-light hydrogen evolution. J. Am. Chem. Soc. 136(5):1730–1733. https://doi.org/10.1021/ja411321s

Sher M, Javed M, Shahid S, Iqbal S, Qamar MA, Bahadur A, Qayyum MA (2021) The controlled synthesis of g-C₃N₄/Cd-doped ZnO nanocomposites as potential photocatalysts for the disinfection and degradation of organic pollutants under visible light

irradiation. RSC Advances 11:2025–2039. https://doi.org/10.1016/j.est.2021.103302

Shi J, Chen G, Zeng G, Chen A, He K, Huang Z, Hu L, Zeng J, Wu J, Liu W (2018) Hydrothermal synthesis of graphene wrapped Fe-doped TiO₂ nanospheres with high photocatalysis performance. Ceram Intl 44:7473–7480. https://doi.org/10.1016/j.ceramint.2018.01.124

Sobhana SSL, Devi M, Sastry T, Mandal A (2011) CdS quantum dots for measurement of the size-dependent optical properties of thiol capping. J. Nanopart. Res. 13:1747–1757. https://doi.org/10.1007/s11051-010-9934-1

Soliman SM, Almarhoon Z, El-Faham A (2019) Synthesis, Molecular and Supramolecular Structures of New Cd(II) Pincer-Type Complexes with s-Triazine Core Ligand. Crystals 9

Song B, Chen M, Ye S, Xu P, Zeng G, Gong J, Li J, Zhang P, Cao W (2019) Effects of multi-walled carbon nanotubes on metabolic function of the microbial community in riverine sediment contaminated with phenanthrene. Carbon 144:1–7. https://doi.org/10.1016/j.carbon.2018.12.016

Tahir M, Cao C, Butt F, Mahmood A, Idrees F, Hussain S, Tanveer M, Ali Z, Aslam I (2013) Multifunctional g-C3N4 nanofibers: a template-free fabrication and enhanced optical, electrochemical, and photocatalyst properties. ACS Appl. Mater. Interfaces 6(2):1258–1265. https://doi.org/10.1021/am405076b

Takanabe K, Kamata K, Wang X, Antonietti M, Kubota J, Domen K (2010) Photocatalytic hydrogen evolution on dye-sensitized mesoporous carbon nitride photocatalyst with magnesium phthalocyanine. Phys Chem Chem Phys: PCCP 12:13020–13025. https://doi.org/10.1039/c0cp00611d

Tarulli SH, Quinzani OV, Piro OE, Castellano EE, Baran EJ (2006) Structural and spectroscopic characterization of bis(thiosaccharinato)bis(benzimidazole)cadmium(II). J Mol Struct 797:56–60

Thaweesak S, Wang S, Lyu M, Xiao M, Peerakiatkhajohn P, Wang L (2017) Boron-doped graphitic carbon nitride nanosheets for enhanced visible-light driven photocatalytic water splitting. Dalton Trans. 46:10714–10720. https://doi.org/10.1039/c7dt00933j

Tonda S, Kumar S, Kandula S, Shanker V (2014) Fe-doped and -mediated graphitic carbon nitride nanosheets for enhanced photocatalytic performance under natural sunlight. J Mater Chem A: Mater Energy Sustain 2:6772. https://doi.org/10.1039/c3ta15358d

Wang Q, Yang Z (2016) Industrial water pollution, water environment treatment, and health risks in China. Environ Pollut 218:358–365. https://doi.org/10.1016/j.envpol.2016.07.011

Wang X, Maeda K, Thomas A, Takanabe K, Xin G, Carlsson J, Domen K, Antonietti M (2008) A metal-free polymeric photocatalyst for hydrogen production from water under visible light. Nature Mater 8:76–80. https://doi.org/10.1038/nmat2317

Wang X, Chen X, Thomas A, Fu X, Antonietti M (2009a) Metal-containing carbon nitride compounds: a new functional organic–metal hybrid material. Adv Mater 21:1609–1612. https://doi.org/10.1002/adma.200802627

Wang X, Maeda K, Thomas A, Takanabe K, Xin G, Carlsson JM, Domen K, Antonietti M (2009b) A metal-free polymeric photocatalyst for hydrogen production from water under visible light. Nature Mater 8:76–80. https://doi.org/10.1038/nmat2317

Wang W, Xu P, Chen M, Zeng G, Zhang C, Zhou C, Yang Y, Huang D, Lai C, Cheng M, Hu L, Xiong W, Guo H, Zhou M (2018a) Alkali metal-assisted synthesis of graphite carbon nitride with tunable band-gap for enhanced visible-light-driven photocatalytic performance. ACS Sustain Chem Eng 6:15503–15516. https://doi.org/10.1021/acssuschemeng.8b03965

Wang Y, Yang W, Chen X, Wang J, Zhu Y (2018b) Photocatalytic activity enhancement of core-shell structure g-C₃N₄@TiO₂ via controlled ultrathin g-C₃N₄ layer. Appl Catal B: Environ 220:337–347. https://doi.org/10.1016/j.apcatb.2017.08.004

Wang Z, Chen M, Huang D, Zeng G, Xu P, Zhou C, Lai C, Wang H, Cheng M, Wang W (2019) Multiply structural optimized strategies for bismuth oxyhalide photocatalysis and their environmental application. Chem Eng J 374:1025–1045. https://doi.org/10.1016/j.cej.2019.06.018

Wang H, Wang H, Wang Z, Tang L, Zeng G, Xu P, Chen M, Xiong T, Zhou C, Li X, Huang D, Zhu Y, Wang Z, Tang J (2020a) Covalent organic framework photocatalysts: structures and applications. Chem Soc Rev 49:4135–4165. https://doi.org/10.1039/d0cs00278j

Wang Z, Wang H, Zeng Z, Zeng G, Xu P, Xiao R, Huang D, Chen X, He L, Zhou C, Yang Y, Wang Z, Wang W, Xiong W (2020b) Metal-organic frameworks derived $Bi_2O_2CO_3$/porous carbon nitride: a nanosized Z-scheme systems with enhanced photocatalytic activity. Appl Catal B: Environ 267:118700. https://doi.org/10.1016/j.apcatb.2020.118700

Wang Z, Han W, Wang Z, Huang D, Qin H, He Y, Chen M, Zeng G, Xu P (2021) Ferrocene modified $g-C_3N_4$ as a heterogeneous catalyst for photo-assisted activation of persulfate for the degradation of tetracycline. Coll Surf A: Physicochem Eng Asp 626:127024. https://doi.org/10.1016/j.colsurfa.2021.127024

Xiang Q, Yu J, Jaroniec M (2012) Synergetic effect of MoS_2 and graphene as cocatalysts for enhanced photocatalytic H_2 production activity of TiO_2 nanoparticles. J Am Chem Soc 134:6575–6578. https://doi.org/10.1016/j.materresbull.2015.12.009

Xiong T, Cen W, Zhang Y, Dong F (2016) Bridging the $g-C_3N_4$ Interlayers for enhanced photocatalysis. ACS Catalysis 6(4):2462–2472. https://doi.org/10.1021/acscatal.5b02922

Xu P, Chen M, Lai C, Zeng G, Huang D, Wang H, Gong X, Qin L, Liu Y, Mo D, Wen X, Zhou C, Wang R (2019) Effects of typical engineered nanomaterials on 4-nonylphenol degradation in river sediment: based on bacterial community and function analysis. Environ Sci: Nano 6:2171–2184. https://doi.org/10.1039/c9en00371a

Xue X, Chen R, Yan C, Hu Y, Zhang W, Yang S, Ma L, Zhu G, Jin Z (2019) Efficient photocatalytic nitrogen fixation under ambient conditions enabled by the heterojunctions of n-type Bi2MoO6 and oxygen-vacancy-rich p-type BiOBr. Nanoscale 11:10439–10445. https://doi.org/10.1039/c9nr02279a

Yan S, Li Z, Zou Z (2009a) Photodegradation performance of $g-C_3N_4$ fabricated by directly heating melamine. Langmuir: ACS J Surf Coll 25:10397–10401. https://doi.org/10.1021/la900923z

Yan SC, Li ZS, Zou ZG (2009b) Photodegradation performance of $g-C_3N_4$ fabricated by directly heating melamine. Langmuir 25:10397–10401. https://doi.org/10.1021/la900923z

Yan S, Li Z, Zou Z (2010) Photodegradation of Rhodamine B and methyl orange over boron-doped $g-C_3N_4$ under visible light irradiation. Langmuir: ACS J Surf Coll 26:3894–3901. https://doi.org/10.1021/la904023j

Yan J, Zhou C, Li P, Chen B, Zhang S, Dong X, Xi F, Liu J (2016) Nitrogen-rich graphitic carbon nitride: controllable nanosheet-like morphology, enhanced visible light absorption and superior photocatalytic performance. Coll Surf A: Physicochem Eng Asp 508:257–264. https://doi.org/10.1016/j.colsurfa.2016.08.067

Yan W, Yan L, Jing C (2019) Impact of doped metals on urea-derived $g-C_3N_4$ for photocatalytic degradation of antibiotics: structure, photoactivity and degradation mechanisms. Appl Catal B: Environ 244:475–485. https://doi.org/10.1016/j.apcatb.2018.11.069

Yang W, Wang J, Pan T, Xu J, Zhang J, Cao C-n (2002) Studies on the electrochemical characteristics of $K_2Sr(FeO_4)_2$ electrode. Electrochem Commun 4:710–715. https://doi.org/10.1016/s1388-2481(02)00429-0

Yang S, Gong Y, Zhang J, Zhan L, Ma L, Fang Z, Vajtai R, Wang X, Ajayan PM (2013) Exfoliated graphitic carbon nitride nanosheets as efficient catalysts for hydrogen evolution under visible light.

Adv Mater 25:2452–2456. https://doi.org/10.1002/adma.201204453

Yu Y, Wang J (2015) Direct microwave synthesis of graphitic C_3N_4 with improved visible-light photocatalytic activity. Ceram Intl 42:4063–4071. https://doi.org/10.1016/j.ceramint.2015.11.078

Yu J, Wang S, Low J, Xiao W (2013) Enhanced photocatalytic performance of direct Z-scheme $g-C_3N_4$–TiO_2 photocatalysts for the decomposition of formaldehyde in air. Phys Chem Chem Phys 15:16883–16890. https://doi.org/10.1039/c3cp53131g

Yu Y, Zhou Q, Wang J (2016) Ultra-rapid synthesis of 2D graphitic carbon nitride nanosheets via direct microwave heating for field emission. Chem. Commun. 52:3396–3399. https://doi.org/10.1039/c5cc10258h

Yu Y, Wang C, Luo L, Wang J, Meng J (2018) An environment-friendly route to synthesize pyramid-like $g-C_3N_4$ arrays for efficient degradation of rhodamine B under visible-light irradiation. Chem Eng J 334:1869–1877. https://doi.org/10.1016/j.cej.2017.11.133

Yuan Y-p, Yin L, Cao S, Gu L, Xu G, Du P, Chai H, Liao Y, Xue C (2014) Microwave-assisted heating synthesis: a general and rapid strategy for large-scale production of high crystalline $g-C_3N_4$ with enhanced photocatalytic H_2 production. Green Chem. 16:4663–4668. https://doi.org/10.1039/c4gc01517g

Yuan J, Liu X, Tang Y, Zeng Y, Wang L, Zhang S, Cai T, Liu Y, Luo S, Pei Y, Liu C (2018) Positioning cyanamide defects in $g-C_3N_4$: Engineering energy levels and active sites for superior photocatalytic hydrogen evolution. Appl Catal B: Environ 237:24–31. https://doi.org/10.1016/j.apcatb.2018.05.064

Zhang L, Xia Z (2011) Mechanisms of oxygen reduction reaction on nitrogen-doped graphene for fuel cells. J Phys ChemC 115(22):11170–11176. https://doi.org/10.1021/jp201991j

Zhang X, Jing D, Guo L (2010) Effects of anions on the photocatalytic H_2 production performance of hydrothermally synthesized Ni-doped $Cd_{0.1}Zn_{0.9}S$ photocatalysts. Intl J Hyd Energy 35:7051–7057. https://doi.org/10.1016/j.ijhydene.2009.12.132

Zhang J, Grzelczak M, Hou Y, Maeda K, Domen K, Fu X, Antonietti M, Wang X (2012) Photocatalytic oxidation of water by polymeric carbon nitride nanohybrids made of sustainable elements. Chem Sci 3:443–446. https://doi.org/10.1039/c1sc00644d

Zhang G, Zhang M, Ye X, Qiu X, Lin S, Wang X (2014) Iodine modified carbon nitride semiconductors as visible light photocatalysts for hydrogen evolution. Adv Mater 26:805–809. https://doi.org/10.1002/adma.201303611

Zhang L, Huang F, Liang C, Zhou L, Zhang X, Pang Q (2016) Ultra-sound exfoliation of $g-C_3N_4$ with assistance of cadmium ions and synthesis of CdS/$g-C_3N_4$ ultrathin nanosheets with efficient photocatalytic activity. J Taiwan Instit Chem Eng 60:643–650. https://doi.org/10.1016/j.jtice.2015.11.013

Zhang C, Lu Y, Jiang Q, Hu J (2016a) Synthesis of CdS hollow spheres coupled with $g-C_3N_4$ as efficient visible-light-driven photocatalysts. Nanotechnology 27:355402. https://doi.org/10.1088/0957-4484/27/35/355402

Zhang C, Lu Y, Jiang Q, Hu J (2016b) Synthesis of CdS hollow spheres coupled with $g-C_3N_4$ as efficient visible-light-driven photocatalysts. Nanotechnology 27:355402. https://doi.org/10.1088/0957-4484/27/35/355402

Zhao Y, Zhao F, Wang X, Xu C, Zhang Z, Shi G, Qu L (2014) Graphitic carbon nitride nanoribbons: graphene-assisted formation and synergic function for highly efficient hydrogen evolution. Angewandte Chemie International Edition 53:13934–13939. https://doi.org/10.1002/ange.201409080

Zhou X, Jin B, Chen R, Peng F, Fang Y (2013) Synthesis of porous Fe_3O_4/$g-C_3N_4$ nanospheres as highly efficient and recyclable photocatalysts. Mater. Res. Bull. 48:1447–1452. https://doi.org/10.1016/j.materresbull.2012.12.038

Zhou W, Li W, Wang J-Q, Qu Y, Yang Y, Xie Y, Zhang K, Wang L, Fu H, Zhao D (2014) Ordered mesoporous Black TiO_2 as

highly efficient hydrogen evolution photocatalyst. J Am Chem Soc 136(26):9280–9283. https://doi.org/10.1021/ja504802q

Zhu Y-P, Ren T-Z, Yuan Z-Y (2015) Mesoporous phosphorus-doped g-C$_3$N$_4$ nanostructured flowers with superior photocatalytic hydrogen evolution performance. ACS Appl Mater Inter 7:16850–16856. https://doi.org/10.1021/acsami.5b04947

Zhu J, Diao T, Wang W, Xu X, Sun X, Carabineiro SAC, Zhao Z (2017) Boron doped graphitic carbon nitride with acid-base duality for cycloaddition of carbon dioxide to epoxide under solvent-free condition. Appl Catal B: Environ 219:92–100. https://doi.org/10.1016/j.apcatb.2017.07.041

Zou J, Yu Y, Yan W, Meng J, Zhang S, Wang J (2019) A facile route to synthesize boron-doped g-C$_3$N$_4$ nanosheets with enhanced visible-light photocatalytic activity. J Mater Sci 54:867–6881. https://doi.org/10.1007/s10853-019-03384-0